Pentraxins Coordinate Excitatory Synapse Maturation and Circuit Integration of Parvalbumin Interneurons

Highlights

- GluA4 is undetectable in neonatal PVFSIs, then increases and plateaus by P15

- $NPTX2^{-/-}/NPTXR^{-/-}$ mice have profound loss of GluA4

- PVFSI AMPAR function and recruitment are compromised in $NPTX2^{-/-}/NPTXR^{-/-}$ mice

- I/E imbalances in $NPTX2^{-/-}/NPTXR^{-/-}$ mice impair rhythmogenesis and working memory

Authors

Kenneth A. Pelkey,
Elizabeth Barksdale, ..., Paul F. Worley,
Chris J. McBain

Correspondence

pelkeyk2@mail.nih.gov

In Brief

Pelkey et al. demonstrate a critical role for neuronal pentraxins 2 and receptor (NPTX2/R) in regulating GluA4 expression within parvalbumin fast-spiking interneurons (PVFSIs). Circuit recruitment of PVFSIs is compromised in $NPTX2^{-/-}/NPTXR^{-/-}$ mice, with consequent deficits in network rhythmogenesis and behavior.

CrossMark

CellPress

Pentraxins Coordinate Excitatory Synapse Maturation and Circuit Integration of Parvalbumin Interneurons

Kenneth A. Pelkey,[1,][*] Elizabeth Barksdale,[1] Michael T. Craig,[1] Xiaoqing Yuan,[1] Madhav Sukumaran,[1] Geoffrey A. Vargish,[1] Robert M. Mitchell,[1] Megan S. Wyeth,[1] Ronald S. Petralia,[2] Ramesh Chittajallu,[1] Rose-Marie Karlsson,[3] Heather A. Cameron,[3] Yasunobu Murata,[4] Matthew T. Colonnese,[4] Paul F. Worley,[5] and Chris J. McBain[1]

[1]Program in Developmental Neuroscience, *Eunice Kennedy-Shriver* National Institute of Child Health and Human Development, National Institutes of Health, 35 Lincoln Drive, Bethesda, MD 20892, USA
[2]Advanced Imaging Core National Institute of Deafness and Other Communication Disorders, National Institutes of Health, 35 Lincoln Drive, Bethesda, MD 20892, USA
[3]Section on Neuroplasticity, Mood and Anxiety Disorders Program, National Institute of Mental Health, National Institutes of Health, 35 Lincoln Drive, Bethesda, MD 20892, USA
[4]Department of Pharmacology and Physiology, and Institute for Neuroscience, George Washington University, 2300 Eye Street, Washington, DC 20037, USA
[5]The Solomon H. Snyder Department of Neuroscience, Johns Hopkins University, 725 N. Wolfe Street, Baltimore, MD 21205, USA
*Correspondence: pelkeyk2@mail.nih.gov
http://dx.doi.org/10.1016/j.neuron.2015.02.020

SUMMARY

Circuit computation requires precision in the timing, extent, and synchrony of principal cell (PC) firing that is largely enforced by parvalbumin-expressing, fast-spiking interneurons (PVFSIs). To reliably coordinate network activity, PVFSIs exhibit specialized synaptic and membrane properties that promote efficient afferent recruitment such as expression of high-conductance, rapidly gating, GluA4-containing AMPA receptors (AMPARs). We found that PVFSIs upregulate GluA4 during the second postnatal week coincident with increases in the AMPAR clustering proteins NPTX2 and NPTXR. Moreover, GluA4 is dramatically reduced in $NPTX2^{-/-}/NPTXR^{-/-}$ mice with consequent reductions in PVFSI AMPAR function. Early postnatal $NPTX2^{-/-}/NPTXR^{-/-}$ mice exhibit delayed circuit maturation with a prolonged critical period permissive for giant depolarizing potentials. Juvenile $NPTX2^{-/-}/NPTXR^{-/-}$ mice display reduced feedforward inhibition yielding a circuit deficient in rhythmogenesis and prone to epileptiform discharges. Our findings demonstrate an essential role for NPTXs in controlling network dynamics highlighting potential therapeutic targets for disorders with inhibition/excitation imbalances such as schizophrenia.

INTRODUCTION

Excitatory afferent recruitment of perisomatic inhibition by PVFSIs dictates synaptic integration properties of downstream excitatory PCs (Pouille and Scanziani, 2001; Gabernet et al., 2005). Such feedforward inhibition provides temporal con-straints upon excitation-spike coupling that allow for coordination of firing rates in PC assemblies (Bartos et al., 2007; Klausberger and Somogyi, 2008). Indeed, depression of AMPA and/or NMDA receptors (AMPAR/NMDAR) selectively within PVFSIs disrupts their recruitment, yielding deficits in PC entrainment that may underlie cognitive deficits associated with psychiatric disorders such as schizophrenia, and predispose circuits to inhibition/excitation (I/E) imbalances that promote epilepsy or Alzheimer's disease (Fuchs et al., 2007; Belforte et al., 2010; Korotkova et al., 2010; Caputi et al., 2012; Maheshwari et al., 2013). However, relative to PCs, little is known regarding establishment and regulation of excitatory synapses onto PVFSIs. Recently, we found that the immediate early gene product neuronal pentraxin 2 (NPTX2; or NARP) regulates synaptic drive selectively onto PVFSIs by promoting activity-dependent accumulation of GluA4-containing AMPARs (Chang et al., 2010). This regulation by NPTX2 critically dictates PVFSI recruitment to maintain circuit I/E balance following perturbations to network activity. The importance of such homeostatic control of PVFSI synaptic integration is highlighted by findings that $NPTX2^{-/-}$ mice display increased sensitivity to kindling-induced epilepsy and fail to exhibit ocular dominance plasticity (Chang et al., 2010; Gu et al., 2013).

Studies revealing a role for NPTX2 in controlling excitatory drive on hippocampal PVFSIs were complicated by the requirement to pretreat mice with stimuli that induce NPTX2 (Chang et al., 2010). In prior studies, this was accomplished by administering maximal electroconvulsive seizures (MECS) 12–18 hr prior to analysis. We sought to avoid the need for MECS, since it will induce other factors that could also contribute to changes in excitability. NPTX2 belongs to the neuronal pentraxin family that also includes the neuronal pentraxin 1 (NPTX1) and neuronal pentraxin receptor/3 (NPTXR/3). All three NPTXs are expressed in adult brain and form disulfide-linked mixed assemblies that bind AMPARs (Xu et al., 2003; Sia et al., 2007). Only NPTX2 is induced by activity (Tsui et al., 1996; Xu et al., 2003). NPTXR is
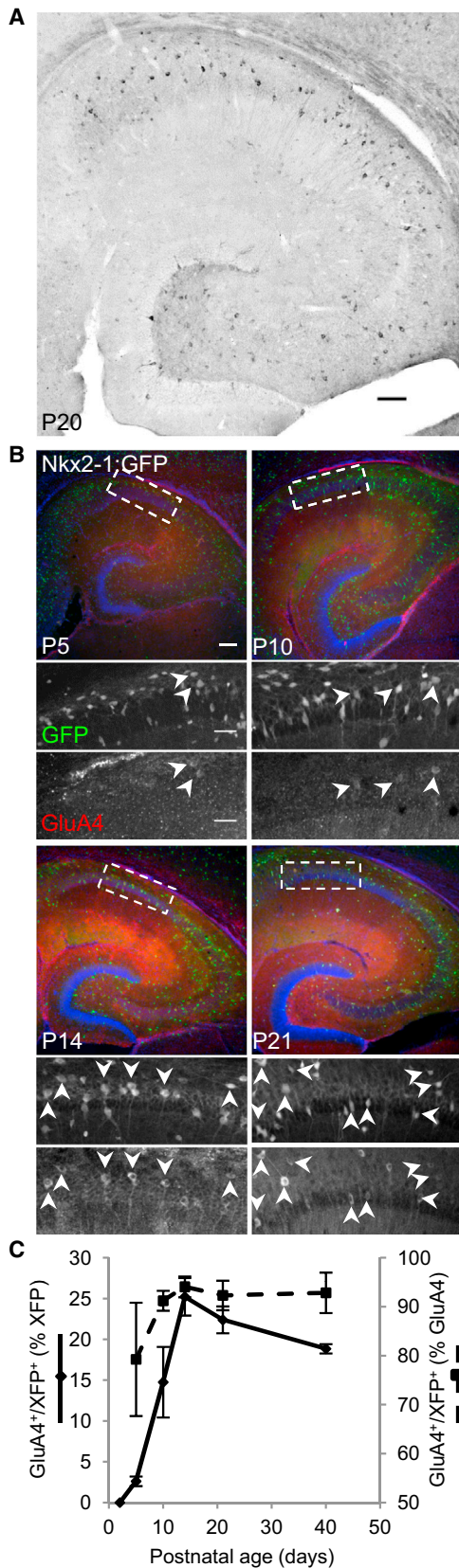
A

P20

B Nkx2-1;GFP

P5   P10

GFP

GluA4

P14   P21

C

Figure 1. Developmental Profile of Hippocampal GluA4 Expression
(A) Representative image illustrating the mature immunolabeling pattern of GluA4 in wild-type hippocampus (scale bar, 100 μm).
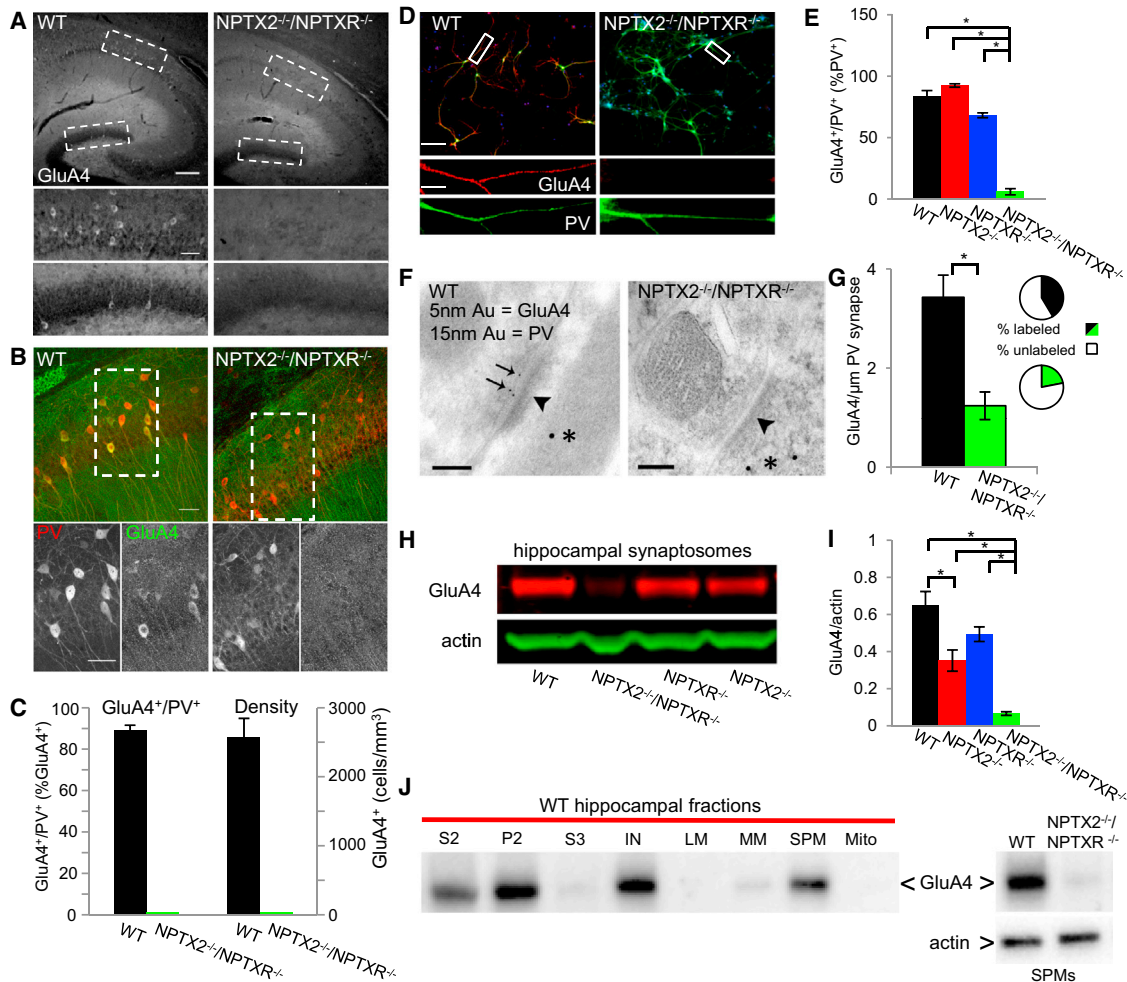(B) Low-magnification (10×) and digitally zoomed panels reveal expression of GFP and GluA4 in representative sections from *Nkx2-1-cre:RCE* mice at the indicated ages (scale bars, 100 and 50 μm for low- and high-magnification images, respectively).
(C) Group data summarizing the developmental expression of GluA4/XFP double-positive cells as percentages of the XFP+ population (solid line, left axis) and GluA4+ population (dashed line, right axis). Mice/sections counted: 2/6, P2; 3/9, P5; 4/10, P10, P14, P21, and P40.

unique in possessing a transmembrane domain and can function to anchor NPTX complexes to plasma membranes. Based on their known cofunctionality, we examined $NPTX2^{-/-}/NPTXR^{-/-}$ mice and found they exhibit basal deficits in PVFSI AMPAR function. Accordingly, $NPTX2^{-/-}/NPTXR^{-/-}$ mice provide a unique opportunity to assess the impact of NPTXs on synapse development, as well as cellular and circuit function, without a requirement for perturbed activity. We report that combined loss of NPTX2 and NPTXR markedly reduces GluA4 expression leading to reduced PVFSI AMPAR function and feedforward inhibition. The resulting I/E imbalance in $NPTX2^{-/-}/NPTXR^{-/-}$ mice disrupts hippocampal rhythmogenesis, promotes epileptic activity, and impairs hippocampal-dependent working memory.

RESULTS AND DISCUSSION

In the mature hippocampus, GluA4-containing AMPARs play an important role at excitatory synapses on PVFSIs due to their fast kinetics and high conductance, which promote efficient synaptic recruitment (Geiger et al., 1995, 1997; Fuchs et al., 2007). This specialized role is highlighted by the limited expression of GluA4 within the mature hippocampus being excluded from PCs and segregated to a sparse population of large cells concentrated around stratum pyramidale of the CA1-CA3 regions and at the hilar-granule cell layer border in the dentate gyrus, consistent with PVFSI localization (Figure 1A). However, early developmental progression of GluA4 in PVFSIs remains largely unknown due to late PV onset (Seto-Ohshima et al., 1990). To address this, we employed *Nkx2-1-cre:RCE* GFP or *Nkx2-1-cre:tdTOM* RFP mice that report the majority of medial ganglionic eminence (MGE)-derived interneurons, including PVFSIs (Tricoire et al., 2010). Immunohistochemical (IHC) analyses revealed the emergence of GluA4+/GFP+ (or RFP+, together considered XFP+) cells at postnatal day 5 (P5), then increasing roughly 10-fold by P14, and leveling off through P40 (Figures 1B and 1C). This contrasts with findings that GluA4 in hippocampal homogenates is high at P1 and then decreases, becoming undetectable by P18 (Zhu et al., 2000), highlighting the importance of cell-type-specific evaluation for minority cell populations within a circuit. However, our findings are consistent with progressive upregulation of GluA4 mRNA within putative PVFSIs over the first 2 postnatal weeks (Okaty et al., 2009). Thus, GluA4 can be grouped together with a number of hallmark proteins expressed by mature PVFSIs such as PV itself, Kv3 channels, synaptotagmin 2, Nav1.1 sodium channels, and

Figure 2. Loss of GluA4 in *NPTX2⁻/⁻/NPTXR⁻/⁻* Mice

(A) GluA4 expression in representative sections from P21 WT and *NPTX2⁻/⁻/NPTXR⁻/⁻* mice (top panels; 10×, scale bar, 200 μm) with zoomed images of CA1 and DG (bottom panels; scale bar, 50 μm).

(B) Representative images illustrating GluA4 and PV expression in CA1 of P21WT and *NPTX2⁻/⁻/NPTXR⁻/⁻* mice (20×, scale bar, 50 μm).

(C) Summary plots of GluA4+/PV+ double-positive cells as percentages of the GluA4+ population (left axis) and the density of GluA4+ cells (right axis) in WT and *NPTX2⁻/⁻/NPTXR⁻/⁻* mice. Mice/sections counted: 5/12, WT; 6/14, *NPTX2⁻/⁻/NPTXR⁻/⁻*.

(D) Representative images of PV (green), GluA4 (red), and DAPI (blue) staining in dissociated hippocampal cultures from wild-type and *NPTX2⁻/⁻/NPTXR⁻/⁻* mice. Low-magnification images (upper, scale bar 150 μm) show merged fluorescence signals, and digitally zoomed panels (lower panels, scale bar, 40 μm) from boxed dendritic regions above highlight GluA4 and PV signals in isolation.

(E) Histogram summarizing the percentage of PV+ cells that express GluA4+ in wild-type, *NPTX2⁻/⁻*, *NPTXR⁻/⁻*, and *NPTX2⁻/⁻/NPTXR⁻/⁻* mice. A total of 127 PV+ cells from 19 culture dishes of wild-type pups from three different litters, 208 PV+ cells from 19 culture dishes of *NPTX2⁻/⁻/NPTXR⁻/⁻* mice from three different litters, 548 PV+ cells from 12 dishes of *NPTX2⁻/⁻* pups from three litters, and 310 PV+ cells from 12 culture dishes from three *NPTXR⁻/⁻* litters were examined, with each litter representing a single n. For each litter paired wild-type and knockout cultures were produced, processed, and analyzed in parallel.

(F) Sample electron micrographs from hippocampal sections of wild-type and *NPTX2⁻/⁻/NPTXR⁻/⁻* mice illustrating asymmetric synapses (arrowheads) in PV immunopositive processes (15 nm gold, *) probed for GluA4 (5 nm gold, arrows in WT) (scale bars, 100 nm).

(G) Histogram summarizing the density of GluA4 immunogold label observed at asymmetric synapses onto PV immunopositive dendrites in wild-type and *NPTX2⁻/⁻/NPTXR⁻/⁻* mice. Insets show the percentage of GluA4 labeled versus unlabeled asymmetric synapses in PV immunopositive processes of wild-type (top) and *NPTX2⁻/⁻/NPTXR⁻/⁻* (bottom) mice. A total of 152 asymmetric synapses from two wild-type mice and a total of 82 asymmetric synapses from three *NPTX2⁻/⁻/NPTXR⁻/⁻* mice were examined.

(H) Representative sample western blots for GluA4, along with β-actin, from hippocampal synaptosomal preparations obtained from wild-type, *NPTX2⁻/⁻*, *NPTXR⁻/⁻*, and *NPTX2⁻/⁻/NPTXR⁻/⁻* mice.

(I) Plotted is a quantitative summary of GluA4 levels in hippocampal synaptosomal preparations from wild-type, *NPTX2⁻/⁻*, *NPTXR⁻/⁻*, and *NPTX2⁻/⁻/NPTXR⁻/⁻* mice. The amount of GluA4 is expressed relative to β-actin, and a total of 18 mice from 14 independent litters for each genotype were paired and analyzed in parallel.

(J) At left is a representative sample immunoblot of discrete biochemical fractions from wild-type hippocampus probed for GluA4 illustrating preferential partitioning of GluA4 into the SPM fraction (S2, postnuclear supernatant; P2, pellet 2; S3, supernatant 3; I, input for sucrose gradient; LM, light membranes; MM,

two-pore domain potassium leak channels (TWIK1 and TASK1/3) that are coordinately upregulated during the first few postnatal weeks and function in a concerted fashion to differentiate immature interneurons fated to become PVFSIs into fast perisomatic targeting inhibitory devices (Du et al., 1996; Doischer et al., 2008; Okaty et al., 2009; Goldberg et al., 2011).

The developmental increase in GluA4 temporally coincides with upregulation of the AMPAR-interacting partners NPTX2 and NPTXR (Cho et al., 2008). Based on their known cofunctionality, we examined the necessity of these NPTXs for normal PVFSI function by probing GluA4 expression in P21-30 mice lacking NPTX2 and NPTXR ($NPTX2^{-/-}/NPTXR^{-/-}$). Surprisingly, specific somatic GluA4 signal was absent throughout the hippocampus of $NPTX2^{-/-}/NPTXR^{-/-}$ mice (Figures 2A–2C). This loss was particularly striking for PV+ cells, which comprised the vast majority of GluA4+ cells in wild-type tissue (Figures 2B and 2C). To confirm the loss of GluA4 throughout $NPTX2^{-/-}/NPTXR^{-/-}$ PVFSIs, we also probed hippocampal cultures. Double labeling for PV and GluA4 confirmed a profound reduction in GluA4 signal throughout the dendritic arbors of PV-expressing cells cultured from $NPTX2^{-/-}/NPTXR^{-/-}$ mice (Figures 2D and 2E). Even when GluA4+ cells were encountered in $NPTX2^{-/-}/NPTXR^{-/-}$ cultures, dendritic expression was comparatively weak (see Figure S1A available online), suggesting that synaptic GluA4 is not spared at the expense of somatic extrasynaptic GluA4. Indeed, subcellular evaluation of GluA4 at asymmetric synapses onto PV immunopositive processes in hippocampal sections confirmed that PVFSIs in $NPTX2^{-/-}/NPTXR^{-/-}$ mice are deficient in synaptic GluA4 content (Figures 2F and 2G). Importantly, GluA4 expression persisted in PV+ cells cultured from either $NPTX2^{-/-}$ or $NPTXR^{-/-}$ mice, and the total number of PV+ cells expressing GluA4 was similar to that of wild-types (Figures 2E and S1A). These observations are consistent with our prior findings of continued GluA4 expression in $NPTX2^{-/-}$ PVFSIs (Chang et al., 2010) and further indicate that $NPTX2$ and $NPTXR$ compensate for each other to some degree in regulating PVFSI GluA4. Indeed, presynaptically derived NPTX2 and NPTXR have both individually been implicated in AMPAR clustering (Sia et al., 2007; Chang et al., 2010). As loss of NPTX2 or NPTXR alone does not lead to compensatory increases of other pentraxins (Bjartmar et al., 2006), residual basal NPTX2 and NPTXR appear capable of driving significant GluA4 expression. Consistent with our IHC findings, biochemical analyses of hippocampal synaptosomal and synaptic plasma membrane preparations (SPMs) further confirmed a dramatic reduction in GluA4 levels in $NPTX2^{-/-}/NPTXR^{-/-}$ mice relative to wild-type and $NPTX2^{-/-}$ or $NPTXR^{-/-}$ mice (Figures 2H–2J). Moreover, loss of GluA4 in $NPTX2^{-/-}/NPTXR^{-/-}$ mice was evident in cerebellum (Figures S1B and S1C), suggesting a conserved role for pentraxins in regulating GluA4 expression throughout the nervous system.

Maturation and circuit integration of PVFSIs has been linked to the formation of perineuronal nets (PNNs) that accumulate preferentially around these cells and control critical period plasticity during network development (Pizzorusso et al., 2002; Gogolla et al., 2009). Interestingly, PNN formation surrounding PVFSIs proceeds with a developmental profile that directly parallels GluA4 expression within PVFSIs (Figures 3A and 3B). Moreover, PNNs are implicated in NPTX2-mediated GluA4 clustering in mature PVFSIs as a homeostatic response to elevated circuit activity (Chang et al., 2010). Thus, it is conceivable that failure of $NPTX2^{-/-}/NPTXR^{-/-}$ PVFSIs to upregulate GluA4 relates to deficient PNN formation. However, we found no difference in PNNs labeled with Wisteria floribunda agglutinin (WFA) surrounding PV+ cells of wild-type and $NPTX2^{-/-}/NPTXR^{-/-}$ hippocampal sections, revealing that NPTX2 and NPTXR are not instructive for PNNs (Figures 3C and 3D). In addition to PNNs, the AMPAR accessory protein stargazin/TARPγ2 is enriched in PVFSIs and has been implicated in regulating PVFSI AMPAR content (Tomita et al., 2003; Maheshwari et al., 2013; Tao et al., 2013). Consistent with these reports, immunoprecipitation of GluA4 from hippocampal synaptic plasma membranes coprecipitates stargazin in wild-type mice (Figure 3E), raising the possibility that the loss of GluA4 in $NPTX2^{-/-}/NPTXR^{-/-}$ mice occurs secondarily to loss of stargazin. Indeed, in stargazin mutant mice GluA4 is reportedly reduced at parallel fiber-interneuron synapses of the cerebellum (Shevtsova and Leitch, 2012) and selectively lost in nucleus reticularis of the thalamus (RTN) (Barad et al., 2012). However, biochemical analyses revealed continued expression of stargazin in the hippocampus of $NPTX2^{-/-}/NPTXR^{-/-}$ mice with preferential partitioning into the SPM fraction similar to wild-type mice (Figure 3F). Moreover, an antibody that recognizes stargazin (and TARPγ8) continues to label $NPTX2^{-/-}/NPTXR^{-/-}$ PV+ cells (Figure 3G), and GluA4 remains present in $stargazin^{-/-}$ mice (Figure S1D). The continued expression of GluA4 in PVFSIs of $stargazin^{-/-}$ mice conflicts with findings at corticothalamic inputs to RTN and may reflect compensation in hippocampal PVFSIs by TARPγ8 which also coprecipitated with hippocampal GluA4 (data not shown). Nonetheless, our findings clearly indicate that loss of GluA4 in $NPTX2^{-/-}/NPTXR^{-/-}$ mice is not related to changes in stargazin. We also probed whether $NPTX2^{-/-}/NPTXR^{-/-}$ mice exhibit altered expression of ErbB4, a receptor tyrosine kinase implicated in PVFSI AMPAR expression and localization (Fazzari et al., 2010; Ting et al., 2011). While ErbB4 was found to interact with GluA4, we did not detect any changes in ErbB4 levels of $NPTX2^{-/-}/NPTXR^{-/-}$ mice (Figures S1E–S1G). Despite the profound reduction of GluA4 protein in $NPTX2^{-/-}/NPTXR^{-/-}$ mice, in situ hybridization and quantitative PCR revealed similar expression of GluA4 mRNA in wild-type and $NPTX2^{-/-}/NPTXR^{-/-}$ mice (Figures 3H–3K). Thus, $NPTX2^{-/-}/NPTXR^{-/-}$ PVFSIs are not deficient in GluA4 transcription, suggesting a role in regulating GluA4 translation or protein stability.

To determine if the loss of GluA4 in $NPTX2^{-/-}/NPTXR^{-/-}$ PVFSIs translates to a functional synaptic deficit, we examined excitatory inputs to PVFSIs. $NPTX2^{-/-}/NPTXR^{-/-}$ mice exhibited a severe reduction in AMPA/NMDA ratios at both granule

microsomal membranes; SPM, synaptic plasma membranes; Mito, mitochondria). At right is a representative sample immunoblot of wild-type and $NPTX2^{-/-}/NPTXR^{-/-}$ SPMs run in parallel and probed for GluA4 (upper blot) and actin (lower blot) illustrating the loss of GluA4 signal in $NPTX2^{-/-}/NPTXR^{-/-}$ hippocampal synapses (SPM GluA4/actin = 5.8 ± 1.3 and 0.57 ± 0.08 for WT and $NPTX2^{-/-}/NPTXR^{-/-}$, respectively; p = 0.02, n = 3 mice per genotype). Values plotted throughout are mean ± SEM; *p < 0.05, Student's t test or Mann-Whitney U Test as appropriate. See also Figure S1.
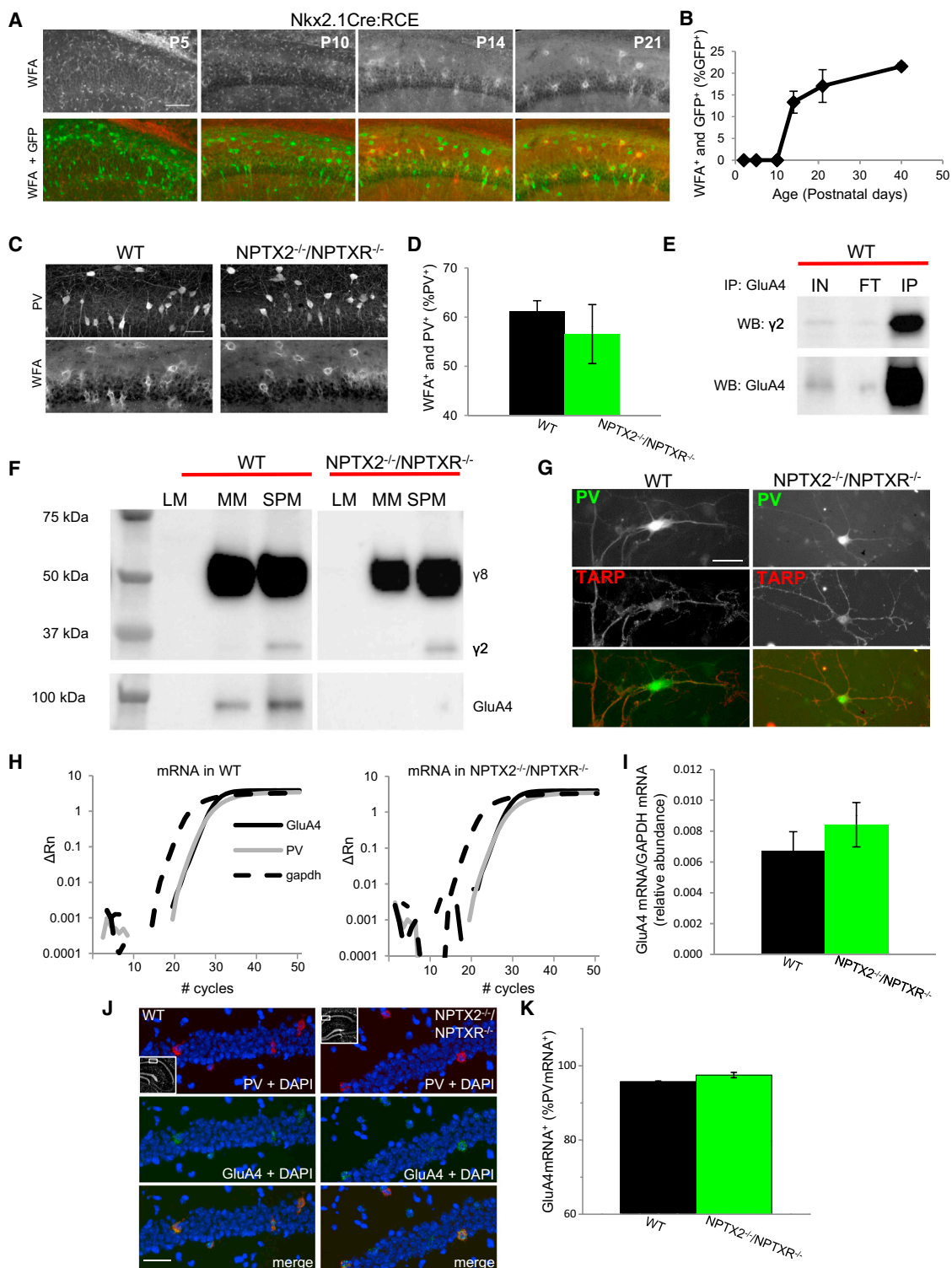
Figure 3. Normal PNN, Stargazin, and GluA4 mRNA Levels in *NPTX2*^{−/−}/*NPTXR*^{−/−} Mice

(A) Representative images of PNN staining with WFA in *Nkx2-1-cre:RCE* hippocampal sections obtained at the developmental time points indicated (scale bar, 100 μm).

(B) Group data plot illustrating the time course for PNN formation around GFP+ cells in *Nkx2-1-cre:RCE* mice. Mice/sections counted: 2/6, P2; 3/3, P5; 2/6, P10; 3/5, P14; 2/6, P21; and 3/5, P40.

(legend continued on next page)

cell- and medial perforant path inputs to PVFSIs (Figures 4A and 4B). This was not accompanied by changes in paired-pulse ratio (PPR) or AMPAR rectification, suggesting that presynaptic function is unaltered and that residual AMPARs remain calcium permeable (Figures 4A and 4B), likely comprised of GluA1 homomers (Geiger et al., 1997). As pentraxins do not interact with NMDARs, the altered AMPA/NMDA ratio in $NPTX2^{-/-}$/$NPTXR^{-/-}$mice likely reflects reduced AMPAR-mediated transmission rather than enhanced NMDAR function. Indeed, AMPAR-mediated spontaneous excitatory postsynaptic currents (sEPSCs) exhibited slower decay kinetics and were reduced in amplitude and frequency in $NPTX2^{-/-}$/$NPTXR^{-/-}$ PVFSIs versus wild-type controls (Figures 4C and 4D). Interestingly, deficits in PVFSI AMPAR function were not observed in either $NPTX2^{-/-}$ or $NPTXR^{-/-}$ single knockouts (Figures 4B and 4D) despite modest decreases in total hippocampal GluA4 probed biochemically (Figure 2I). This lack of synaptic phenotype in single knockouts is consistent with our prior findings (Chang et al., 2010) and the continued expression of GluA4 in most PVFSIs of $NPTX2^{-/-}$ or $NPTXR^{-/-}$ mice (Figure 2E).

Reduced AMPAR function in PVFSIs is expected to disrupt efficient synaptic recruitment of these cells and thus compromise feedforward perisomatic inhibition, promoting a circuit I/E imbalance in downstream PCs (Pouille and Scanziani, 2001; Gabernet et al., 2005). To probe whether reduced AMPAR function in $NPTX2^{-/-}$/$NPTXR^{-/-}$ PVFSIs alters I/E balance, we examined disynaptic inhibition in the Schaffer collateral-CA1 pyramidal cell (SC-CA1 PC) circuit. Compared to wild-types, $NPTX2^{-/-}$/$NPTXR^{-/-}$ mice exhibited reduced feedforward inhibition when normalized to monosynaptic excitation in SC-CA1 PC recordings (Figures 4E and 4F). As SC-CA1 PC excitation was not different between wild-type and $NPTX2^{-/-}$/$NPTXR^{-/-}$ slices (inset, Figure 4F), the altered I/E ratio reflects a reduction in recruited inhibition rather than increased excitatory drive at SC-CA1 synapses. Importantly, total density of PVFSIs was comparable between wild-type and $NPTX2^{-/-}$/$NPTXR^{-/-}$ mice, indicating that similar numbers of PVFSIs are available for recruitment in the two genotypes (PV+ cell density of $NPTX2^{-/-}$/$NPTXR^{-/-}$ was 91% ± 7% of that observed in wild-types, e.g., Figures 2B and 3C). Indeed, the developmental trajectory of hippocampal PV expression was similar in wild-type and $NPTX2^{-/-}$/$NPTXR^{-/-}$mice (Figures S2A and S2B).

Moreover, basic membrane properties of $NPTX2^{-/-}$/$NPTXR^{-/-}$ PVFSIs were comparable to wild-types (Figures 4G and 4H). Finally, PVFSI GABA release probed with the oxytocin receptor agonist TGOT, which selectively drives PVFSI firing (Owen et al., 2013), was similar in wild-type and $NPTX2^{-/-}$/$NPTXR^{-/-}$ slices (Figures 4I and 4J). Thus, reduced disynaptic inhibition in $NPTX2^{-/-}$/$NPTXR^{-/-}$ mice likely reflects diminished PVFSI afferent-driven recruitment due to impaired AMPAR function within these cells rather than deficits in PVFSI numbers, impaired spike generation, or transmitter release. Interestingly, the reduced PVFSI AMPAR function and consequent disruption of feedforward inhibition in $NPTX2^{-/-}$/$NPTXR^{-/-}$ are similar in magnitude to observations in $GluA4^{-/-}$ mice (Fuchs et al., 2007). This is consistent with the almost complete absence of GluA4 in $NPTX2^{-/-}$/$NPTXR^{-/-}$ mice and reinforces the critical role of NPTXs in regulating GluA4 expression to control PVFSI circuit integration.

Failure of circuits to effectively recruit PVFSIs and the ensuing I/E imbalance has the capacity to disrupt coherent population activity, since PVFSIs critically entrain PC assemblies (Bartos et al., 2007; Klausberger and Somogyi, 2008). Thus, we next probed physiological and pathological hippocampal network activity in $NPTX2^{-/-}$/$NPTXR^{-/-}$ mice. We first examined the immature hippocampus beginning on postnatal day 6 (P6) when circuit activity is dominated by giant depolarizing potentials (GDPs). GDPs occur spontaneously in immature networks to drive correlated population activity and are paced by depolarizing GABAergic inhibition prior to the onset of mature chloride gradients within PCs (Ben-Ari et al., 2007). In recordings from CA3 PCs, we reliably observed GDPs in wild-type and $NPTX2^{-/-}$/$NPTXR^{-/-}$ mice between P6 and P8 in every PC examined (Figures 5A–5D). Then between P9 and P13 the occurrence of GDPs decreased in both genotypes, but with distinct temporal dynamics (Figure 5C). In wild-types less than 50% of CA3 PCs exhibited GDPs at P11, and no GDPs were detected beyond this age. In contrast, greater than 50% of the PCs examined in $NPTX2^{-/-}$/$NPTXR^{-/-}$ mice still exhibited GDPs at P12, yielding a significant increase in the overall frequency of GDPs across all recordings at P11-P12 (Figure 5D). This altered time course of GDPs within the $NPTX2^{-/-}$/$NPTXR^{-/-}$ hippocampus is reminiscent of disrupted critical period plasticity and synaptic refinement in the developing visual system of pentraxin-deficient mice

(C and D) Representative images (C) and group data (D) illustrating the colocalization of PNNs and PV+ cells in hippocampal sections obtained from P21–P30 wild-type and $NPTX2^{-/-}$/$NPTXR^{-/-}$ mice (scale bar, 35 μm). Mice/sections counted: 5/5, WT; 2/5, $NPTX2^{-/-}$/$NPTXR^{-/-}$.

(E) Representative immunoblots illustrating that pull-down of GluA4 from hippocampal synaptic plasma membranes coprecipitates stargazin (γ2) as well as GluA4 itself (IP lanes). Also shown are the input (IN) and flowthrough (FT) materials probed with the same antibodies (comparing FT/IN signals revealed that 55% ± 9% of available SPM stargazin coprecipitated with GluA4, n = 4 mice).

(F) Representative western blots of the indicated cell fractions from wild-type and $NPTX2^{-/-}$/$NPTXR^{-/-}$ hippocampi probed with an antibody that recognizes stargazin (γ2) and TARPγ8 (γ8; upper blot) or GluA4 (lower blot). SPM stargazin/actin = 0.38 ± 0.06 and 0.34 ± 0.06 for wild-type and $NPTX2^{-/-}$/$NPTXR^{-/-}$ mice, respectively, p = 0.66, n = 3 mice per genotype.

(G) Representative images of PV+ cells from wild-type and $NPTX2^{-/-}$/$NPTXR^{-/-}$ mice cultures confirming stargazin/γ8 expression in PV+ cells in both genotypes (scale bar, 50 μm).

(H) Representative single-trial qPCR amplification plots for GluA4 mRNA (solid black), PV (gray), and GADPH (hashed black) from wild-type and $NPTX2^{-/-}$/$NPTXR^{-/-}$ hippocampi. Relative fluorescence intensities (deltaR$_n$) are plotted against PCR cycle numbers on a logarithmic scale.

(I) Group data summarizing the abundance of GluA4 mRNA (relative to GADPH) in hippocampi from wild-type and $NPTX2^{-/-}$/$NPTXR^{-/-}$ mice. Three independent experiments using RNA from three independent litters of each genotype were performed.

(J and K) Representative sample images (J) and group data summary (K) of wild-type and $NPTX2^{-/-}$/$NPTXR^{-/-}$ hippocampal sections probed for PV and GluA4 mRNA by fluorescent in situ hybridization (scale bar, 50 μm). Cells/sections/mice counted: 165/4/2, WT; 196/6/3, $NPTX2^{-/-}$/$NPTXR^{-/-}$. See also Figure S1.
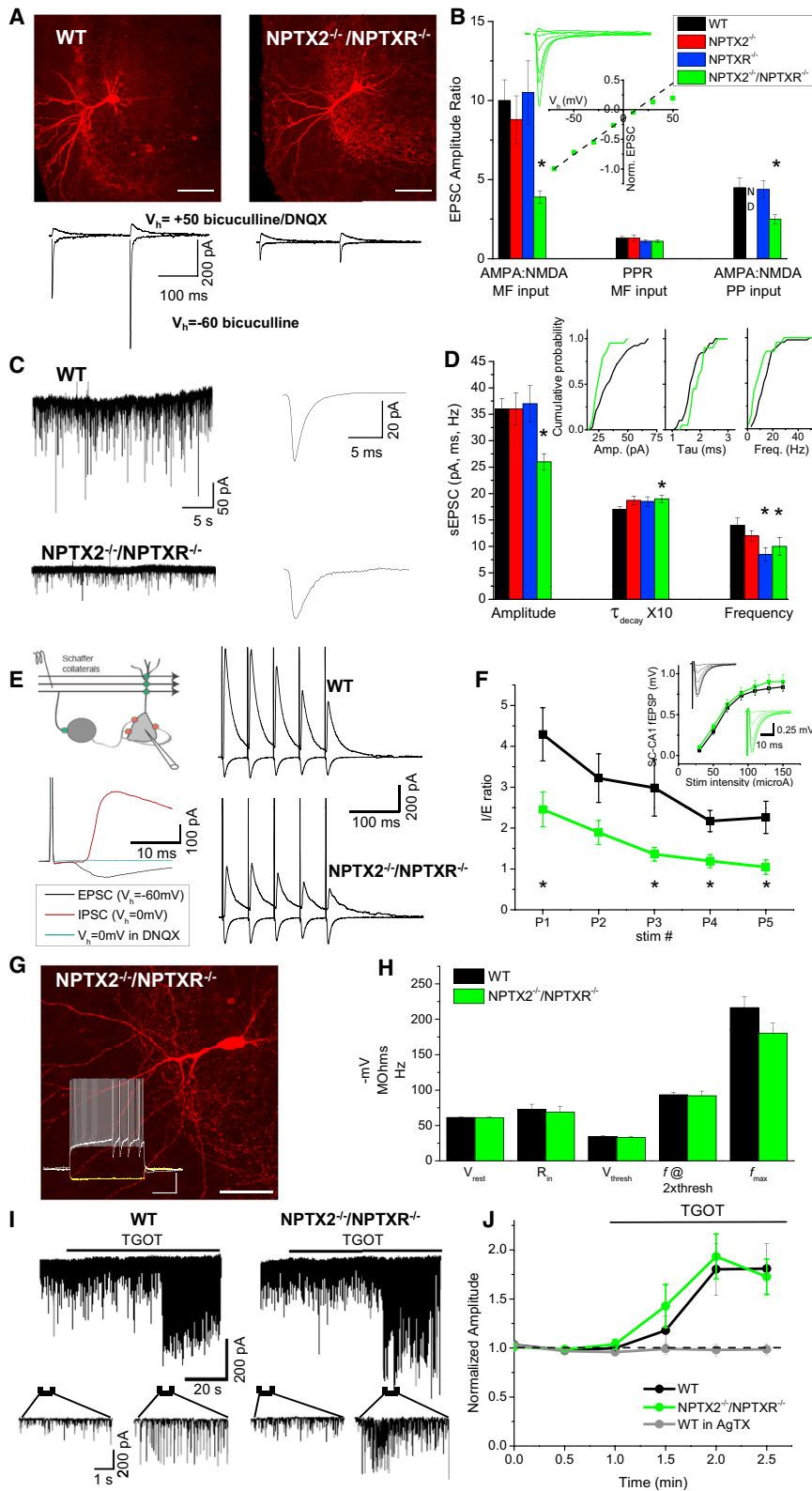
Figure 4. Impaired PVFSI AMPAR Function and Feedforward Inhibition in *NPTX2⁻/⁻/NPTXR⁻/⁻* Mice

(A) Representative PVFSIs recorded in wild-type and *NPTX2⁻/⁻/NPTXR⁻/⁻* mice with corresponding AMPA and NMDA EPSC traces evoked by granule cell stimulation (scale bars, 100 μm).

(B) Summary for AMPA/NMDA ratios in PVFSIs at granule cell (MF, n = 16 cells/8 mice, 4 cells/4 mice, 8 cells/5 mice, 15 cells/7 mice for WT, *NPTX2⁻/⁻*, *NPTXR⁻/⁻*, *NPTX2⁻/⁻/NPTXR⁻/⁻*, respectively; *p = 0.00007 versus WT, Mann-Whitney U test) and medial perforant path (PP, n = 15 cells/6 mice, 6 cells/3 mice, 7 cells/3 mice for WT, *NPTXR⁻/⁻*, and *NPTX2⁻/⁻/NPTXR⁻/⁻*, respectively; *p = 0.02 versus WT Mann-Whitney U test) inputs for indicated genotypes (PP inputs not determined [ND] for *NPTX2⁻/⁻* mice). Also plotted are PPRs (5 Hz) of MF-PVFSI EPSCs. Inset, I–V relation for AMPAR-mediated transmission, and sample traces, at PP inputs to *NPTX2⁻/⁻/NPTXR⁻/⁻* PVFSIs (n = 5 cells/3 mice).

(C) Representative sEPSC recordings (left) and ensemble average sEPSC (right) recorded in WT and *NPTX2⁻/⁻/NPTXR⁻/⁻* PVFSIs.

(D) Summary of PVFSI sEPSC properties for the indicated genotypes (n = 39 cells/16 mice, 23 cells/8 mice, 14 cells/7 mice, 20 cells/9 mice for WT, *NPTX2⁻/⁻*, *NPTXR⁻/⁻*, and *NPTX2⁻/⁻/NPTXR⁻/⁻*, respectively; *p = 0.002, 0.03, 0.01, and 0.01 for amplitude, Tau$_{decay}$, frequency (blue bar), and frequency (green bar), respectively, versus WT) and cumulative probability plots comparing WT and *NPTX2⁻/⁻/NPTXR⁻/⁻* PVFSIs (insets).

(E) Schematic (above, left) and sample traces (below, left) illustrating methodology for recording SC-CA1 feedforward inhibition, along with representative sample recordings in wild-type and *NPTX2⁻/⁻/NPTXR⁻/⁻* mice (right).

(F) Group data summary plot of I/E ratios observed using train stimulation in wild-type and *NPTX2⁻/⁻/NPTXR⁻/⁻* mice (n = 10 cells/3 mice and 9 cells/3 mice for wild-type and *NPTX2⁻/⁻/NPTXR⁻/⁻*, respectively; p = 0.04, 0.005, 0.02, and 0.008 for P1, P3, P4, and P5, respectively, Mann-Whitney U test). Inset shows SC-CA1 excitatory field potential recording (fEPSP) input-output relations, with traces from representative recordings, for wild-type and *NPTX2⁻/⁻/NPTXR⁻/⁻* mice.

(G) Image of a representative *NPTX2⁻/⁻/NPTXR⁻/⁻* dentate PVFSI (scale bar, 100 μm) and associated voltage responses (lower inset) to hyperpolarizing current injection (−200 pA) as well as depolarizing current injections perithreshold (250 pA) and twice perithreshold (500 pA) for action potential firing (inset scale bars, 250 ms/20 mV).

(H) Histogram summarizing resting membrane potentials (V$_{rest}$), input resistances (R$_{in}$), action potential thresholds (V$_{thresh}$), firing frequencies at twice threshold current injection (f @2Xthresh), and maximal firing frequencies (f$_{max}$) measured in wild-type (n = 16 cells/7 mice) and *NPTX2⁻/⁻/NPTXR⁻/⁻* (n = 9 cells/4 mice) PVFSIs.

(I) Continuous traces (upper) from representative CA1 PC recordings in wild-type (left) and *NPTX2⁻/⁻/NPTXR⁻/⁻* (right) mice illustrating the effects of oxytocin receptor agonist ([Thre⁴, Gly⁷]-oxytocin, TGOT) treatment to evoke release from PVFSIs on sIPSCs. Traces below show the indicated regions on an expanded timescale.

(legend continued on next page)

(Bjartmar et al., 2006; Koch and Ullian, 2010; Gu et al., 2013), suggesting a general role for synaptic integration of PVFSIs in coordinating circuit maturation.

Despite the prolonged developmental window to observe GDPs in $NPTX2^{-/-}/NPTXR^{-/-}$ mice, other GDP features, including frequency at younger ages, duration, and charge transfer, were comparable to those of wild-type mice, indicating similar synaptic dynamics underlying GDP emergence and pacing in both genotypes (Figures 5D–5F). Indeed, GDP frequency in both wild-type and $NPTX2^{-/-}/NPTXR^{-/-}$ mice was sensitive to modulation by cannabinoid and NMDA receptor tone, as previously reported (Figures 5G and 5H) (Ben-Ari et al., 1989; Bernard et al., 2005). Thus, rather than directly participating in the cellular and synaptic mechanisms that drive GDPs, PVFSIs likely function to terminate the permissive window for GDP generation, perhaps by triggering the establishment of hyperpolarizing chloride gradients following initiation of perisomatic innervation (Ben-Ari et al., 2007). This model is consistent with pacing of GDPs by dendritic inhibition rather than perisomatic inhibition (Ben-Ari et al., 2007), a feature highlighted by the strong regulation by cannabinoid receptors which likely operate at dendrite-targeting, cholecystokinin-expressing interneurons (Morozov and Freund, 2003; Lee et al., 2010).

Cessation of the critical period for GDP generation in the maturing hippocampus signals a transition from spontaneously internal circuit-generated network activity to mature oscillatory patterns driven by behavior such as sensory processing, spatial navigation, learning, and memory retrieval. Unlike GDPs, pacing of mature network rhythms critically relies upon PVFSI-mediated perisomatic inhibition to entrain PC assemblies, particularly in the gamma frequency range (Bartos et al., 2007; Klausberger and Somogyi, 2008). To determine whether changes in I/E balance observed in $NPTX2^{-/-}/NPTXR^{-/-}$ mice alters circuit rhythmogenesis in juvenile mice, we examined carbachol (CCh)-induced gamma oscillations (Mann et al., 2005). Field recordings in the CA3 PC layer of hippocampal slices revealed that gamma power was markedly impaired in $NPTX2^{-/-}/NPTXR^{-/-}$ slices compared to interleaved wild-type slices (Figures 6A–6F). Consistent with our PVFSI synaptic analyses, gamma power in $NPTX2^{-/-}$ and $NPTXR^{-/-}$ single knockout mice was comparable to wild-types (Figures 6C and 6D). While average peak gamma frequency was similar between the four genotypes (Figure 6E), both $NPTXR^{-/-}$ and $NPTX2^{-/-}/NPTXR^{-/-}$ mice had greater variability in gamma frequency, indicating less stable oscillations (Figure 6F). The minor phenotype in the absence of just $NPTXR^{-/-}$ may reflect a small deficit in excitatory drive onto PVFSIs relating to reduced sEPSC frequency in this mouse (Figure 4D).

To determine whether naturally occurring in vivo oscillations are disrupted in $NPTX2^{-/-}/NPTXR^{-/-}$ mice, we performed extracellular recordings from hippocampal CA1 in awake, head-fixed mice. Analyses of the local field potential recorded in stratum pyramidale revealed clear episodes of theta and gamma activity during active states in aged-matched wild-type and $NPTX2^{-/-}/NPTXR^{-/-}$ mice, indicating that these rhythms remain intact in the mutants (e.g., Figures 6G and 6H). However, examination of the averaged power spectra across all recordings revealed deficient power in the gamma frequency range of $NPTX2^{-/-}/NPTXR^{-/-}$ mice compared to wild-types (Figure 6I). Indeed, further analysis confirmed a significant reduction in peak gamma power of $NPTX2^{-/-}/NPTXR^{-/-}$ mice that was accompanied by a modest decrease in peak gamma frequency (Figures 6J and 6K). In contrast, peak theta power was similar between wild-type and $NPTX2^{-/-}/NPTXR^{-/-}$ mice, though the mutants exhibited a small reduction in peak theta frequency (Figures 6L and 6M).

In addition to theta and gamma oscillations, we also observed sharp wave-associated ripple events (SWRs) during periods of quiet wakefulness in wild-type and $NPTX2^{-/-}/NPTXR^{-/-}$ mice (e.g., Figures 7A and 7B). These high-frequency oscillations (125–250 Hz) are thought to drive memory consolidation during periods of immobility, consummatory behaviors, and slow wave sleep by allowing rapid network replay of exploratory driven activity patterns over compressed time periods (Buzsáki, 1986; Foster and Wilson, 2006). Of particular relevance to the current study, PVFSIs are implicated in coordinating the ensembles of PCs that participate in SWRs (Csicsvari et al., 1999a, 1999b; Ellender et al., 2010). Indeed, among the hippocampal oscillatory rhythms examined in awake behaving mice, SWRs induce the greatest depth of PVFSI firing modulation (Varga et al., 2012, 2014). Overall, we found that the incidence of SWRs in $NPTX2^{-/-}/NPTXR^{-/-}$ mice was reduced compared to wild-types (Figure 7C). Analysis of individual SWRs using Morlet wavelets (e.g., Figures 7D and 7E) revealed that SWRs in wild-type and $NPTX2^{-/-}/NPTXR^{-/-}$ mice had similar durations, peak amplitudes, and peak power, but that SWRs in $NPTX2^{-/-}/NPTXR^{-/-}$ mice were reduced in peak frequency (Figures 7F–7I). Importantly, the laminar profiles of sharp waves and associated ripples were normal in $NPTX2^{-/-}/NPTXR^{-/-}$ mice (e.g., Figures 7A and 7B), excluding the possibility that the deficits observed related to changes in the depth profiles of the recordings.

In general, our in vitro and in vivo network findings are consistent with previous reports that mouse mutants with reduced glutamatergic drive onto PVFSIs display altered hippocampal oscillations (Fuchs et al., 2007; Rácz et al., 2009; Belforte et al., 2010; Korotkova et al., 2010; Caputi et al., 2012; Carlén et al., 2012). In particular, mice with targeted deletion of GluA4 exhibit compromised kainate-induced gamma oscillations in vitro, similar to our observations for CCh-induced gamma oscillations in $NPTX2^{-/-}/NPTXR^{-/-}$ mice (Fuchs et al., 2007). Moreover, ablation of GluA4 selectively in hippocampal PVFSIs reduces SWR occurrence and decreases peak frequency similar to our current findings in $NPTX2^{-/-}/NPTXR^{-/-}$ mice (Caputi et al., 2012). Thus, $NPTX2^{-/-}/NPTXR^{-/-}$ mice phenocopy several network features of $GluA4^{-/-}$ knockouts. However, in

(J) Summary time course plot of the effects of TGOT on sIPSC amplitudes in wild-type (n = 6 cells from 3 mice) and $NPTX2^{-/-}/NPTXR^{-/-}$ (n = 7 cells from 3 mice) CA1 PCs. sIPSC amplitudes measured during 30 s epochs during TGOT treatment were normalized to the average amplitude measured prior to TGOT application. Also plotted is the effect of TGOT in wild-type CA1 PCs treated with omega-agatoxin (AgTX, 500 nM; n = 4 cells from 2 mice) to prevent release from PVFSIs, confirming that TGOT selectively drives sIPSC output from PVFSIs (Hefft and Jonas, 2005; Owen et al., 2013). Values plotted throughout are average ± SEM. Recordings throughout were made in slices from mice aged P15–P30. See also Figure S2.
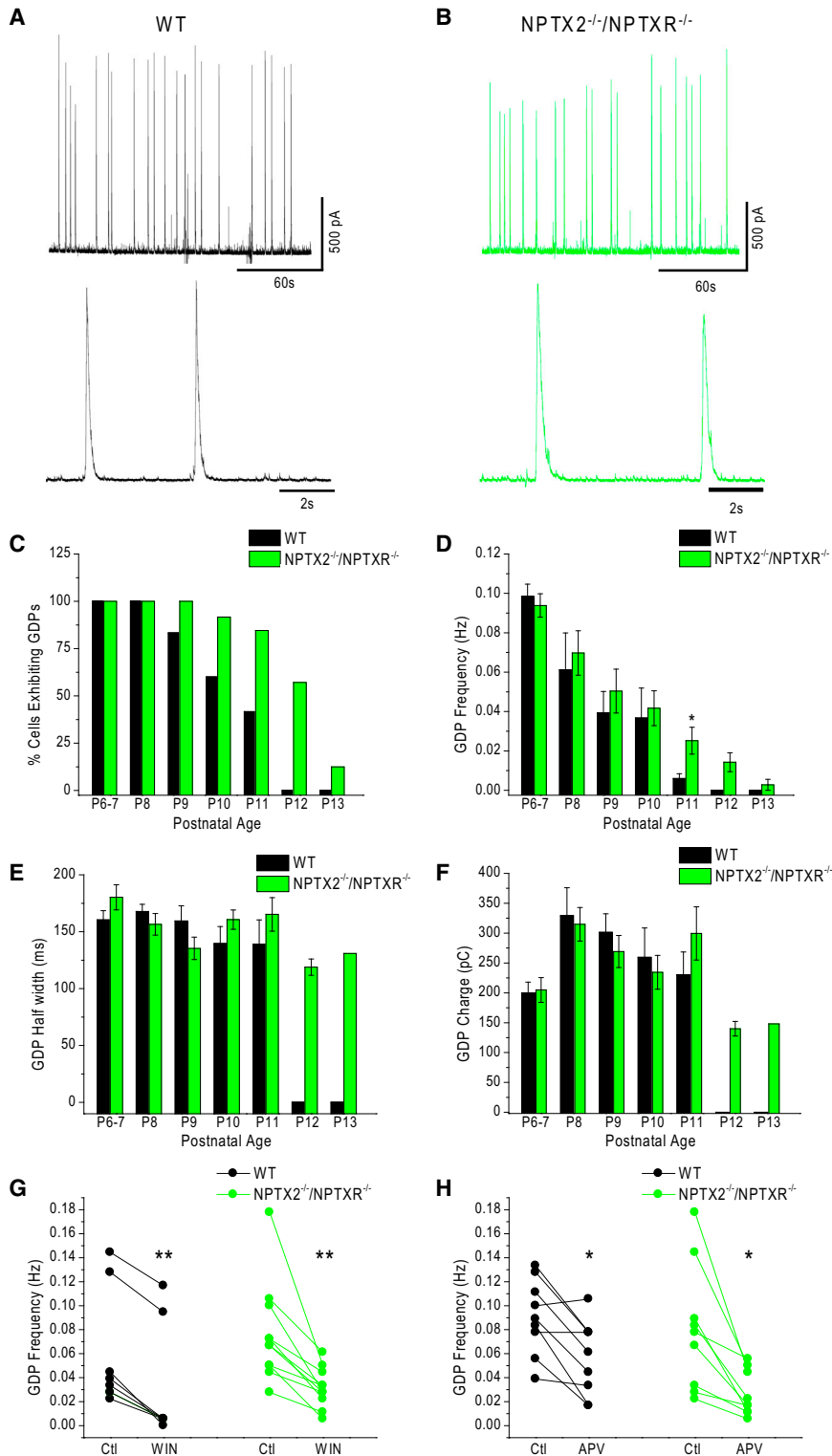
Figure 5. Prolonged Critical Period for GDP Expression in $NPTX2^{-/-}/NPTXR^{-/-}$ Mice

(A and B) Representative sample traces illustrating GDPs recorded in slices from wild-type (A) and $NPTX2^{-/-}/NPTXR^{-/-}$ mice with individual GDPs illustrated below on an expanded timescale.

(C–F) Histograms summarizing the developmental profiles (ages indicated along x axis) for the percentage of CA3 PCs exhibiting GDPs (C), GDP frequency averaged across recorded cells for each stage of development (D), GDP half-widths observed across development (E), and the average total charge transferred through GDPs at each stage of development (F) in wild-type and $NPTX2^{-/-}/NPTXR^{-/-}$ slices. For wild-type recordings the total number of cells and mice recorded at each time point (P6–P7 to P13) were 15/3, 7/2, 12/2, 10/2, 12/2, 11/3, and 6/1; and for $NPTX2^{-/-}/NPTXR^{-/-}$ mice, 19/3, 18/3, 14/2, 24/3, 13/2, 14/2, 8/1. (D) *p = 0.015, Mann-Whitney U test. Note, as GDPs were not observed at P12 and P13 in wild-type mice we did not perform any statistical comparisons with GDP properties of $NPTX2^{-/-}/NPTXR^{-/-}$ mice at these stages.

(G and H) Summary plots illustrating the effects of cannabinoid receptor antagonism with WIN 55,212-2 mesylate (WIN, 5 μM) and NMDAR antagonism with DL-APV (APV, 100 μM) on GDP frequencies in wild-type and $NPTX2^{-/-}/NPTXR^{-/-}$ mice. Plotted are GDP frequencies observed in each recording before (Ctl) and after WIN or APV treatment. (G) **p = 0.007 and 9.7×10^{-4} for WT and $NPTX2^{-/-}/NPTXR^{-/-}$, respectively (Wilcoxon test). (H) *p = 0.026 and 0.015 for wild-type and $NPTX2^{-/-}/NPTXR^{-/-}$, respectively (paired t test).

To investigate potential behavioral consequences of the circuit defects in $NPTX2^{-/-}/NPTXR^{-/-}$ mice, we examined their performance in a series of tasks designed to probe general exploration, anxiety, and spatial working memory. In the novel open field test, $NPTX2^{-/-}/NPTXR^{-/-}$ mice exhibited increased exploratory activity relative to wild-types during the first 5 min of the test, but reduced exploration toward the end of a 60 min session, indicating more rapid habituation (Figure 7J). This habituation phenotype of $NPTX2^{-/-}/NPTXR^{-/-}$ mice yielded an overall decrease in exploration compared to wild-types throughout the entire session consistent with findings in $GluA4^{-/-}$ mice (Fuchs et al., 2007). Despite their increased initial locomotion, $NPTX2^{-/-}/NPTXR^{-/-}$ mice spent less time than controls exploring the center

contrast to our findings in $NPTX2^{-/-}/NPTXR^{-/-}$ mice, PVFSI $GluA4^{-/-}$ mice did not exhibit in vivo gamma oscillation deficits and displayed decreases in SWR peak amplitude and power (Caputi et al., 2012).

area of the open field during the first 10 min, consistent with an anxiety-like phenotype (Figure 7K). Indeed, subsequent evaluation in the elevated O-maze revealed that mutant mice spent less time than controls in the open arms confirming anxiety-like
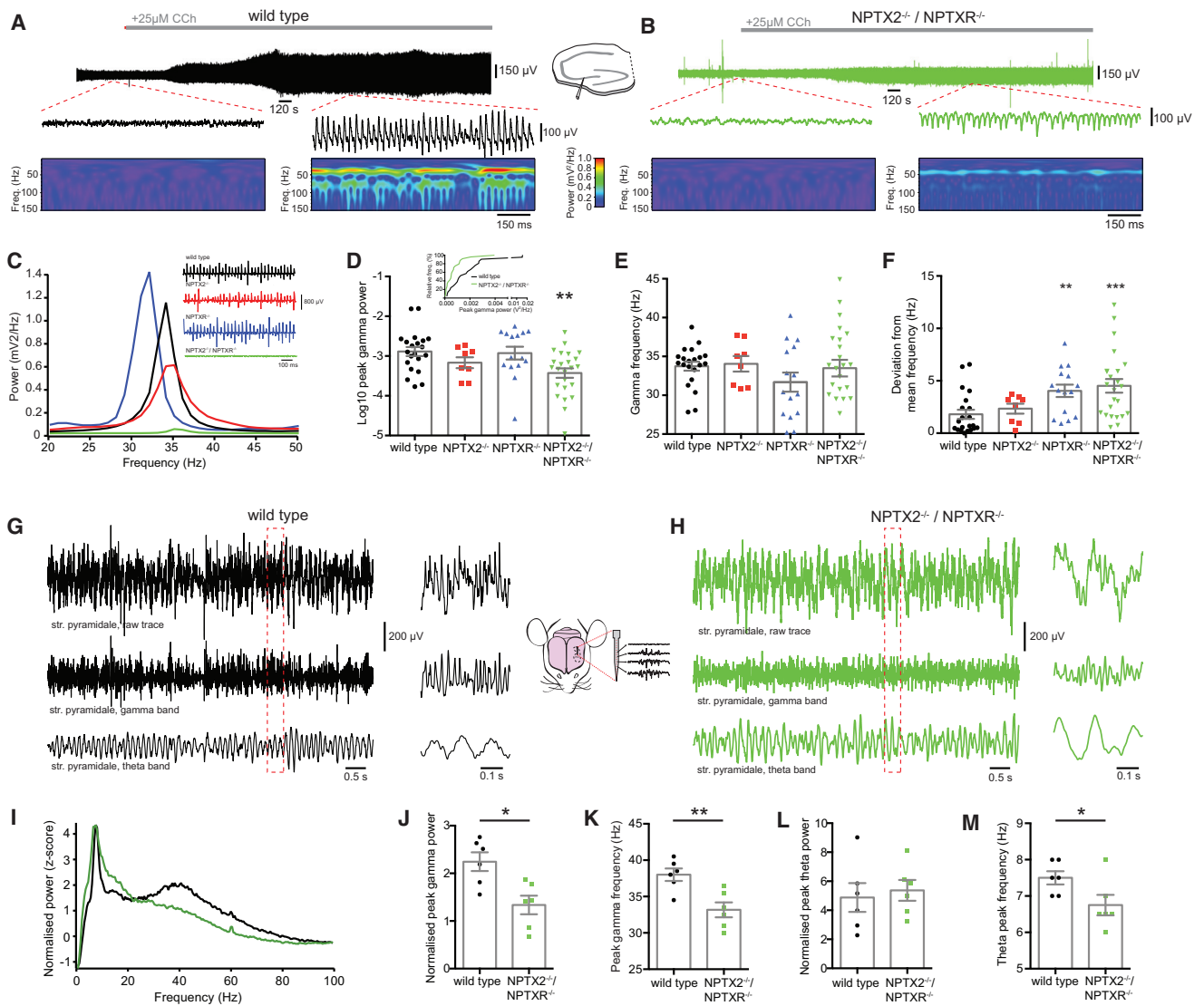
Figure 6. Impaired Gamma Oscillations in NPTX2⁻/⁻/NPTXR⁻/⁻ Mice Both In Vitro and In Vivo

(A and B) In vitro gamma oscillations detected in field recordings (top and middle) from CA3 in slices from wild-type (A) or *NPTX2⁻/⁻/NPTXR⁻/⁻* (B) mice after bath application of 25 μM carbachol (CCh), with corresponding wavelet transform (bottom).

(C) Power density spectra from representative recordings of CCh-evoked gamma oscillations in wild-type (black), *NPTX2⁻/⁻* (red), *NPTXR⁻/⁻* (blue), and *NPTX2⁻/⁻/NPTXR⁻/⁻* (green) mice. Inset shows corresponding sample traces.

(D) *NPTX2⁻/⁻/NPTXR⁻/⁻* mice had significant gamma oscillation deficits (Log$_{10}$ peak gamma power, WT [n = 21] versus *NPTX2⁻/⁻* [n = 8] versus *NPTXR⁻/⁻* [n = 15] versus *NPTX2⁻/⁻/NPTXR⁻/⁻* [n = 24]; −2.89 ± 0.11 versus −3.17 ± 0.14 versus −2.92 ± 0.16 versus −3.43 ± 0.12; p = 0.0074, one-way ANOVA with post hoc Bonferroni multiple comparisons); inset shows cumulative frequency distributions of the peak gamma power for WT and *NPTX2⁻/⁻/NPTXR⁻/⁻* mice.

(E) No significant differences in peak gamma frequency were observed (WT versus *NPTX2⁻/⁻* versus *NPTXR⁻/⁻* versus *NPTX2⁻/⁻/NPTXR⁻/⁻*: 33.7 ± 0.75 Hz versus 34.1 ± 1.00 Hz versus 31.7 ± 1.23 Hz versus 33.5 ± 1.07 Hz; *F* = 0.898, p = 0.447, one-way ANOVA).

(F) *NPTXR⁻/⁻* and *NPTX2⁻/⁻/NPTXR⁻/⁻* mice displayed significantly greater variability in gamma frequency (deviation from mean frequency, WT versus *NPTX2⁻/⁻* versus *NPTXR⁻/⁻* versus *NPTX2⁻/⁻/NPTXR⁻/⁻*: 1.80 ± 0.43 Hz versus 2.34 ± 0.47 Hz versus 4.04 ± 0.59 Hz versus 4.51 ± 0.65 Hz; *H* = 16.64, p = 0.0008, Kruskal-Wallis test with post hoc Dunn's multiple comparisons test).

(G and H) Representative in vivo recordings from CA1 stratum pyramidale of wild-type (G) or *NPTX2⁻/⁻/NPTXR⁻/⁻* (H) mice, showing raw traces (top), the same traces band-pass filtered between 25 and 90 Hz to show the gamma band (middle) and band-pass filtered between 5 and 10 Hz to show the theta band (bottom). Traces at right with expanded timescale are from boxed regions of the longer time-compressed traces.

(I) Normalized power spectra, averaged from all mice in wild-type (black, n = 6) or *NPTX2⁻/⁻/NPTXR⁻/⁻* (green, n = 6) groups.

(J and K) (J) *NPTX2⁻/⁻/NPTXR⁻/⁻* mice displayed a significant reduction in peak gamma power (z-score, WT versus *NPTX2⁻/⁻/NPTXR⁻/⁻*: 2.13 ± 0.27 versus 1.34 ± 0.20; *t* = 2.410; p = 0.0367; Student's t test) and (K) peak gamma frequency WT versus *NPTX2⁻/⁻/NPTXR⁻/⁻*: 38.0 ± 0.86 versus 33.2 ± 1.03; *t* = 3.608; p = 0.0048; Student's t test).

(legend continued on next page)

behavior (Figure 7L). Finally, we found that NPTX2$^{-/-}$/NPTXR$^{-/-}$ made significantly fewer correct choices across multiple trials in the rewarded T-maze alternation task, suggesting impaired hippocampus-dependent working memory (Figure 7M). This deficit in spatial working memory of NPTX2$^{-/-}$/NPTXR$^{-/-}$ mice likely relates directly to the loss of GluA4 within PVFSIs, as several prior studies have reported deficits in working memory following genetic manipulations that compromise PVFSI function (Fuchs et al., 2007; Belforte et al., 2010; Korotkova et al., 2010; Murray et al., 2011; Caputi et al., 2012; Carlén et al., 2012).

Previously we found that NPTX2$^{-/-}$ mice display increased sensitivity to kindling-induced epilepsy (Chang et al., 2010). As NPTX2$^{-/-}$ mice cannot homeostatically increase PVFSI GluA4, we postulated that this phenotype reflects failure of NPTX2$^{-/-}$ circuits to rebalance network I/E dynamics and suppress epileptogenesis early in the kindling protocol. Importantly, NPTX2$^{-/-}$ mice showed identical initial responses to kindling but diverged from wild-types as the kindling process evolved (Chang et al., 2010), consistent with normal baseline GluA4 content and circuit integration of PVFSIs in NPTX2$^{-/-}$ mice. In contrast, the severe basal deficit of PVFSI synaptic recruitment in NPTX2$^{-/-}$/NPTXR$^{-/-}$ mice predicts a basal epilepsy phenotype. However, NPTX2$^{-/-}$/NPTXR$^{-/-}$ mice did not exhibit overt seizures, nor did we detect any electrophysiological features of epilepsy during hippocampal in vivo recordings. To further assess acute epileptiform sensitivity of wild-type, NPTX2$^{-/-}$, NPTXR$^{-/-}$, and NPTX2$^{-/-}$/NPTXR$^{-/-}$ mice, we monitored hippocampal network activity while challenging slices with a modest increase in extracellular potassium (to 8.5 mM; Traynelis and Dingledine, 1988). In adult rat slices, this challenge typically promotes spontaneous recurring interictal bursting, with a minority of slices ($\sim$20%) progressing to electrographic seizure-like activity comprised of ictal events reminiscent of discharges recorded in vivo during tonic-clonic seizures (Traynelis and Dingledine, 1988). Similarly, in our recordings wild-type, NPTX2$^{-/-}$, and NPTXR$^{-/-}$ slices all consistently exhibited spontaneous interictal bursting within 7–10 min of increased [K$^+$]$_o$ with only a minority of slices yielding ictal events (Figures 8A, 8C, and 8D). In contrast, slices from NPTX2$^{-/-}$/NPTXR$^{-/-}$ consistently displayed full-blown epileptiform activity producing spontaneous ictal activity with characteristic tonic and clonic bursts at regular intervals (Figures 8B and 8D). Pooling of data across all recordings revealed that ictal frequency is significantly enhanced in NPTX2$^{-/-}$/NPTXR$^{-/-}$ compared to wild-type mice, while interictal frequency is significantly lower in NPTX2$^{-/-}$/NPTXR$^{-/-}$ due to the excess time spent in ictal discharges (Figures 8C and 8D). While data from NPTX2$^{-/-}$ and NPTXR$^{-/-}$ single knockouts trended toward intermediate phenotypes, slices from these lines were not significantly different from wild-types.

Considering our findings of GluA4 loss and deficient synaptic drive in NPTX2$^{-/-}$/NPTXR$^{-/-}$ PVFSIs, the increased epileptiform sensitivity of slices from these mice likely stems from deficient recruitment of perisomatic inhibition leading to network

hyperexcitability. This interpretation is consistent with evidence that GluA4 mutant mice serve as an animal model of absence epilepsy (Paz et al., 2011). However, our synaptic findings indicate that despite the reduced circuit integration of PVFSIs in NPTX2$^{-/-}$/NPTXR$^{-/-}$ mice these cells still exhibit some capacity for afferent recruitment and once engaged provide efficient GABAergic input to PCs (cf. Figures 4 and 5). Thus, we reasoned that the epilepsy-like phenotype of NPTX2$^{-/-}$/NPTXR$^{-/-}$ mice might be sensitive to an increase in the efficacy of GABAergic tone from the PVFSIs engaged in a blunted fashion during the epileptiform activity. To test this, we utilized the GABA$_A$ receptor-positive allosteric modulator indiplon that is selective for alpha1-containing receptors which are preferentially, though not solely, localized postsynaptic to PVFSI inputs (Klausberger et al., 2002; Petroski et al., 2006). Following initiation of epileptiform activity in NPTX2$^{-/-}$/NPTXR$^{-/-}$ slices, indiplon eliminated ictal activity in 50% of recordings tested and reduced ictal frequency in the remaining slices (Figures 8E and 8F). Following indiplon, interictal events remained as the dominant activity similar to wild-type, NPTX2$^{-/-}$, and NPTXR$^{-/-}$ mice, indicating that the underlying pacemaker synaptic drive engaged by high [K$^+$]$_o$ was not disrupted (e.g., Figure 8E). Rather, indiplon reversal of epileptiform activity likely proceeds by enhancing circuit inhibition, including but not limited to PVFSI-mediated perisomatic inhibition to improve I/E balance. This rescue of the NPTX2$^{-/-}$/NPTXR$^{-/-}$ epileptiform phenotype is consistent with the ability of optogenetic-mediated recruitment of PVFSIs to arrest spontaneous seizures in vivo (Krook-Magnuson et al., 2013) and further validates PVFSI-mediated inhibition as an effective therapeutic target for disorders precipitated by circuit I/E imbalance.

In summary, we have uncovered an essential role for NPTX2 and NPTXR in orchestrating the basic developmental program for synaptic integration and network function of hippocampal PVFSIs. The coincidental temporal relation of NPTX2, NPTXR, and GluA4 expression, combined with loss of GluA4 in NPTX2$^{-/-}$/NPTXR$^{-/-}$ mice, suggests these NPTXs regulate PVFSI circuit integration by controlling expression and synaptic localization of GluA4-containing AMPARs. Although GluA4 levels are upregulated in concert with a number of other proteins that are also critical for promoting speed and precision in PVFSI function such as PV, Kv3 channels, Nav1.1 sodium channels, and two-pore domain potassium leak channels (TWIK1 and TASK1/3), our findings suggest normal developmental progression of these other proteins in NPTX2$^{-/-}$/NPTXR$^{-/-}$ mice. Thus, within PVFSIs, pentraxins serve to selectively drive maturation of AMPAR function by facilitating the production of GluA4. Given the reduction in PVFSI sEPSC frequency it is also possible that NPTXs serve a synaptogenic function in PVFSIs and that NPTX2$^{-/-}$/NPTXR$^{-/-}$ mice have reduced numbers of excitatory synaptic contacts onto them. However, overall dendritic architectures of PVFSIs were similar in wild-type and NPTX2$^{-/-}$/NPTXR$^{-/-}$ mice, and the mutants exhibited only modest

---

(L and M) (L) NPTX2$^{-/-}$/NPTXR$^{-/-}$ mice did not display significant differences in peak theta power (z-score, WT versus NPTX2$^{-/-}$/NPTXR$^{-/-}$: 4.38 ± 1.01 versus 5.37 ± 0.71; t = 0.7938; p = 0.4457, Student's t test) but (M) did display a small but significant decrease in peak theta frequency (WT versus NPTX2$^{-/-}$/NPTXR$^{-/-}$: 7.50 ± 0.18 versus 6.75 ± 0.28; t = 2.236; p = 0.0493; Student's t test). *p < 0.05, **p < 0.01, ***p < 0.001 versus wild-type. In vitro recordings were performed in slices from mice aged P15–P21, and in vivo recordings were performed in P32–P34 mice.
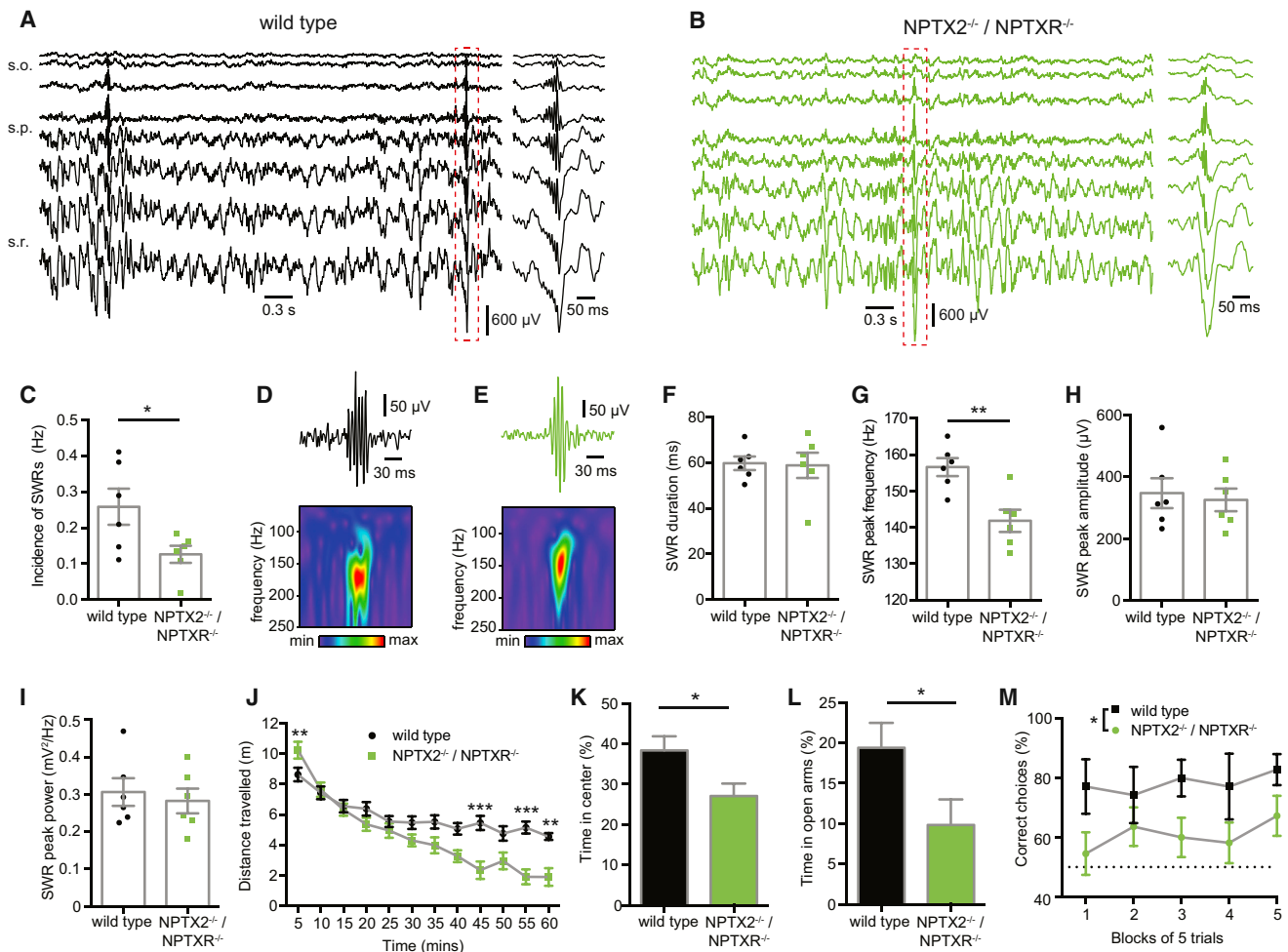
Figure 7. Altered SWRs and Behavioral Deficits in *NPTX2⁻/⁻/NPTXR⁻/⁻* Mice

(A and B) Depth profiles (interelectrode distance of 50 μm) of representative recordings illustrating SWRs in (A) wild-type and (B) *NPTX2⁻/⁻/NPTXR⁻/⁻* mice in vivo.

(C) The incidence of SWRs was significantly reduced in *NPTX2⁻/⁻/NPTXR⁻/⁻* mice (WT [n = 6] versus *NPTX2⁻/⁻/NPTXR⁻/⁻* [n = 6], 0.26 ± 0.05 Hz versus 0.13 ± 0.02 Hz; p = 0.0387; Student's t test).

(D and E) Examples of sharp wave ripples from (D) wild-type and (E) *NPTX2⁻/⁻/NPTXR⁻/⁻* mice, recorded from stratum pyramidale, band-pass filtered (130–250 Hz, top) with corresponding wavelet transforms of the raw traces (bottom).

(F) *NPTX2⁻/⁻/NPTXR⁻/⁻* mice did not display a significant difference in the SWR duration (WT versus *NPTX2⁻/⁻/NPTXR⁻/⁻*: 59.7 ± 2.96 ms versus 58.8 ± 5.5 ms; p = 0.8880; Student's t test).

(G–I) (G) *NPTX2⁻/⁻/NPTXR⁻/⁻* mice did show a significant reduction in the peak frequency of SWRs (WT versus *NPTX2⁻/⁻/NPTXR⁻/⁻*: 157 ± 2.47 Hz versus 142 ± 3.05 Hz; p = 0.0037; Student's t test). *NPTX2⁻/⁻/NPTXR⁻/⁻* mice did not display a significant difference in either (H) SWR amplitude (WT versus *NPTX2⁻/⁻/NPTXR⁻/⁻*: 348 ± 48.2 μV versus 326 ± 36.6 μV; t = 0.3622; p = 0.7247; Student's t test) or (I) SWR power (peak power, mV²/Hz, WT versus *NPTX2⁻/⁻/NPTXR⁻/⁻*: 0.31 ± 0.04 versus 0.28 ± 0.03; t = 0.4777; p = 0.6431; Student's t test).

(J) *NPTX2⁻/⁻/NPTXR⁻/⁻* showed early open-field locomotor hyperactivity and late hypoactivity (n = 15 WT and 13 *NPTX2⁻/⁻/NPTXR⁻/⁻* mice; genotype × time interaction: $F_{1,26}$ = 7.8620, p = 0.0094; two-way ANOVA).

(K and L) (K) *NPTX2⁻/⁻/NPTXR⁻/⁻* displayed increased anxiety-like behavior in (K) the novel open field (t = 2.3810, p = 0.0248; Student's t test). (L) Anxiety-like behavior was confirmed in the elevated O-maze (n = 15 mice per genotype; t = 2.1624, p = 0.0393; Student's t test).

(M) *NPTX2⁻/⁻/NPTXR⁻/⁻* mice made fewer correct choices in a reward alternation task (n = 7 WTs and 11 mutants; main effect of genotype; $F_{1,16}$ = 7.7876, p = 0.0131; two-way ANOVA) *p < 0.05 **p < 0.01, ***p < 0.001 versus wild-type. In vivo recordings were performed in P32–P34 mice, and behavior was assessed in P70–P91 mice.

reductions in synaptic density (Figures S2C–S2J). Thus, the deficits in *NPTX2⁻/⁻/NPTXR⁻/⁻* PVFSI recruitment relate primarily to reduced AMPAR content at synapses rather than dramatic changes in the numbers of afferents impinging upon PVFSIs.

Prior studies have focused on the role of neuronal pentraxins as AMPAR clustering proteins without evidence of a larger role in coordinating both overall protein expression and synaptic localization (O'Brien et al., 1999, 2002; Mi et al., 2002; Xu
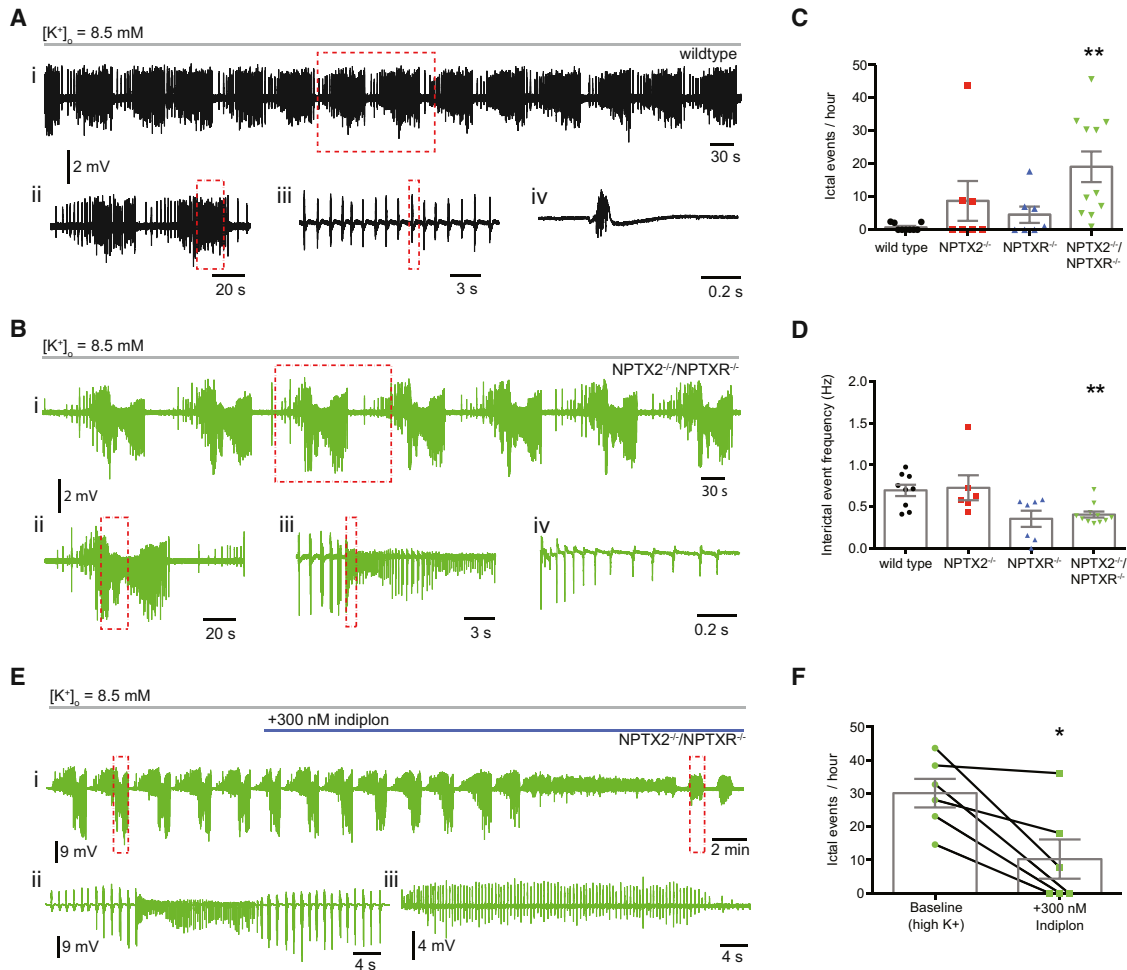
Figure 8. Increased Susceptibility to Epileptiform Activity in *NPTX2⁻/⁻/NPTXR⁻/⁻* Mice

(A) Representative recordings of epileptiform activity induced following bath application of 8.5 mM $[K^+]_o$ in slices from wild-type mice: (i) representative trace from WT mouse showing rhythmic clusters of interictal events; (ii) two clusters of interictal events from boxed region of i on an expanded timescale; (iii) expanded timescale trace from boxed area in (ii), showing rhythmicity of interictal events; (iv) single interictal event from boxed area of (iii) on expanded timescale.

(B) Similar to (A), but for a representative *NPTX2⁻/⁻/NPTXR⁻/⁻* recording: (i) representative trace from *NPTX2⁻/⁻/NPTXR⁻/⁻* mouse showing rhythmic clusters of ictal events; (ii) single ictal event from boxed region in (i) on expanded timescale; (iii) boxed event from (ii) on expanded timescale with interictal events preceding the onset of an ictal event; (iv) beginning of ictal event on an expanded timescale from boxed region in iii.

(C) *NPTX2⁻/⁻/NPTXR⁻/⁻* mice displayed significantly more ictal events during high K^+ epileptiform activity (ictal events per hour, WT (n = 9) versus *NPTX2⁻/⁻* (n = 7) versus *NPTXR⁻/⁻* (n = 7) versus *NPTX2⁻/⁻/NPTXR⁻/⁻* (n = 11): 0.78 ± 0.39 versus 8.77 ± 6.05 versus 4.60 ± 2.48 versus 19.12 ± 4.64; H = 13.85, p = 0.0031, Kruskal-Wallis test with post hoc Dunn's multiple comparisons test).

(D) Interictal events in *NPTX2⁻/⁻/NPTXR⁻/⁻* mice were significantly less frequent (interictal event frequency, WT versus *NPTX2⁻/⁻* versus *NPTXR⁻/⁻* versus *NPTX2⁻/⁻/NPTXR⁻/⁻*: 0.70 ± 0.07 Hz versus 0.73 ± 0.15 Hz versus 0.35 ± 0.10 Hz versus 0.41 ± 0.04 Hz; p = 0.0033, Kruskal-Wallis test with post hoc Dunn's multiple comparisons test).

(E) Representative recording from an *NPTX2⁻/⁻/NPTXR⁻/⁻* slice showing the effect of indiplon on high K^+-induced ictal activity. Shown is a full time course of indiplon-mediated attenuation of ictal events (i) with a single ictal event prior to indiplon application (ii) and remaining interictal events (iii) after indiplon from the boxed regions in (i) shown on expanded timescales.

(F) Bath application of indiplon significantly reduced the frequency of ictal events in *NPTX2⁻/⁻/NPTXR⁻/⁻* mice (ictal events per hour, baseline versus indiplon [n = 6]: 30.0 ± 4.3 versus 10.3 ± 5.9; p = 0.0141; paired t test. **p < 0.01 versus WT). Recordings throughout were performed in P15–P30 mice.

et al., 2003; Sia et al., 2007; Chang et al., 2010). Interestingly, GluA4 transcription proceeds normally in the absence of NPTX2 and NPTXR. Given the direct association of neuronal pentraxins with the N-terminal domain of GluA4, it is possible that this interaction stabilizes GluA4 to prevent rapid degradation. Alternatively, pentraxins may regulate GluA4 mRNA transla-

tion. Future studies into the cellular mechanisms of NPTX-mediated GluA4 regulation will be necessary to resolve these possibilities. Concerning the sources of NPTX2 and NPTXR for regulating PVFSI GluA4, evidence to date implicates presynaptically derived NPTXs in driving synaptic AMPAR accumulation (Chang et al., 2010; Sia et al., 2007). While NPTX2 is secreted,

the transmembrane domain of NPTXR may serve to anchor NPTX complexes at presynaptic terminals innervating PVFIs. Such heterocomplexes may then be released to interact with postsynaptic PVFSIs following activity-dependent cleavage of NPTXR by extracellular matrix metalloproteases (Cho et al., 2008). An alternate possibility would place NPTXR in the postsynaptic membrane of PVFIs to bind presynaptically derived NPTX2. However, while activity-dependent NPTX2 expression has recently been demonstrated in somatostatin interneurons (Spiegel et al., 2014), NPTX expression has not yet been localized within PVFIs.

Previously, NPTX2 alone was implicated in homeostatic adaptations in GluA4 levels and AMPAR function (Chang et al., 2010). However, $NPTX2^{-/-}$ PVFSIs exhibit normal basal excitatory drive. Thus, $NPTX2^{-/-}/NPTXR^{-/-}$ mice provided a unique opportunity to assess the impact of NPTXs on cellular and circuit function, without a requirement for perturbed activity. Indeed, we found that $NPTX2^{-/-}/NPTXR^{-/-}$ mice exhibited basal deficits in PVFSI AMPAR function, yielding a circuit with reduced feedforward inhibition and disrupted network oscillations and that is prone to epileptiform activity. In association with these circuit changes, $NPTX2^{-/-}/NPTXR^{-/-}$ mice exhibited increased anxiety-like behavior as well as deficits in exploration and spatial working memory. These cellular, network, and behavioral deficiencies are similar to findings in GluA4 mutants (Fuchs et al., 2007; Paz et al., 2011), indicating that the reduction of GluA4 in $NPTX2^{-/-}/NPTXR^{-/-}$ mice is sufficient in magnitude to phenocopy mice with targeted deletion of GluA4. Our current findings extend the role of NPTXs to coordinating the basic synaptic developmental program of PVFSIs, and reveal the essential role of NPTXs in controlling hippocampal network properties. The restricted expression of GluA4 to PVFSIs, combined with the selective synaptic regulation by NPTXs, points to the importance of these targets for understanding and treating disorders associated with I/E imbalance due to PVFSI dysfunction.

EXPERIMENTAL PROCEDURES

Detailed experimental procedures are provided in Supplemental Information.

IHC, Cell Culture, and Postembedding EM
Fixed brains from mice P2–P60 were removed, cryoprotected, and sectioned, then stained for the indicated proteins with visualization either using fluorescently labeled secondary Abs or through immunoperoxidase labeling. Images of the stained sections were obtained, and labeled cells were manually counted, with the results converted to cell-density measurements. Hippocampal cell cultures were prepared from P0–P5 mice, and fixation and staining were performed after 15–30 days in vitro. Postembedding immunogold EM was performed on tissue from 2-month-old mice with excitatory synapse density and synaptic GluA4 content evaluated in PV immunopositive processes.

Biochemistry, qPCR, and ISH
Western blot analyses were performed on hippocampal synaptosomes and membrane fractions or cerebellar lysates obtained from P22-P30 mice as indicated. For quantification, densitometry of protein bands of interest was normalized to that of β-actin. Immunoprecipitations were performed from SPM fractions run through GluA4-conjugated beads. qPCR was carried out on P20 hippocampi using a StepOne instrument from Applied Biosystems, and target gene levels were normalized to the endogenous control gene gadph. ISH was carried out on fresh frozen sections from P30 mice using the RNAscope Fluorescent Multiplex kit (Advanced Cell Diagnostics Inc.).

Electrophysiology and Behavior
Whole-cell patch recordings from PVFSIs and CA1/CA3 pyramids were performed in submerged hippocampal slices from P5–P30 mice to evaluate PVFSI synaptic/intrinsic/spiking properties, feedforward inhibition, and GDPs as indicated. For in vitro gamma oscillations and epileptiform activity, CA3 local field potentials (LFPs) were recorded in slices maintained in an interface chamber. In vivo recordings were performed in awake head-fixed mice (P32–P34) using a 32 channel electrode inserted into the hippocampus through a craniotomy to monitor CA1 LFPs. For behavior, adult mice (10–13 weeks old) were assessed for novelty-induced locomotor activity in a novel square arena, anxiety-like behavior in an elevated O-maze, and spatial working memory using rewarded alternation in a T-maze.

REFERENCES

Barad, Z., Shevtsova, O., Arbuthnott, G.W., and Leitch, B. (2012). Selective loss of AMPA receptors at corticothalamic synapses in the epileptic stargazer mouse. Neuroscience 217, 19–31.

Bartos, M., Vida, I., and Jonas, P. (2007). Synaptic mechanisms of synchronized gamma oscillations in inhibitory interneuron networks. Nat. Rev. Neurosci. 8, 45–56.

Belforte, J.E., Zsiros, V., Sklar, E.R., Jiang, Z., Yu, G., Li, Y., Quinlan, E.M., and Nakazawa, K. (2010). Postnatal NMDA receptor ablation in corticolimbic interneurons confers schizophrenia-like phenotypes. Nat. Neurosci. 13, 76–83.

Ben-Ari, Y., Cherubini, E., Corradetti, R., and Gaiarsa, J.L. (1989). Giant synaptic potentials in immature rat CA3 hippocampal neurones. J. Physiol. 416, 303–325.

Ben-Ari, Y., Gaiarsa, J.L., Tyzio, R., and Khazipov, R. (2007). GABA: a pioneer transmitter that excites immature neurons and generates primitive oscillations. Physiol. Rev. 87, 1215–1284.

Bernard, C., Milh, M., Morozov, Y.M., Ben-Ari, Y., Freund, T.F., and Gozlan, H. (2005). Altering cannabinoid signaling during development disrupts neuronal activity. Proc. Natl. Acad. Sci. USA 102, 9388–9393.

Bjartmar, L., Huberman, A.D., Ullian, E.M., Rentería, R.C., Liu, X., Xu, W., Prezioso, J., Susman, M.W., Stellwagen, D., Stokes, C.C., et al. (2006). Neuronal pentraxins mediate synaptic refinement in the developing visual system. J. Neurosci. 26, 6269–6281.

Buzsáki, G. (1986). Hippocampal sharp waves: their origin and significance. Brain Res. 398, 242–252.

Caputi, A., Fuchs, E.C., Allen, K., Le Magueresse, C., and Monyer, H. (2012). Selective reduction of AMPA currents onto hippocampal interneurons impairs network oscillatory activity. PLoS ONE 7, e37318.

Carlén, M., Meletis, K., Siegle, J.H., Cardin, J.A., Futai, K., Vierling-Claassen, D., Rühlmann, C., Jones, S.R., Deisseroth, K., Sheng, M., et al. (2012). A critical role for NMDA receptors in parvalbumin interneurons for gamma rhythm induction and behavior. Mol. Psychiatry 17, 537–548.

Chang, M.C., Park, J.M., Pelkey, K.A., Grabenstatter, H.L., Xu, D.S., Linden, D.J., Sutula, T.P., McBain, C.J., and Worley, P.F. (2010). Narp regulates homeostatic scaling of excitatory synapses on parvalbumin-expressing interneurons. Nat. Neurosci. 13, 1090–1097.

Cho, R.W., Park, J.M., Wolff, S.B., Xu, D., Hopf, C., Kim, J.A., Reddy, R.C., Petralia, R.S., Perin, M.S., Linden, D.J., and Worley, P.F. (2008). mGluR1/5-dependent long-term depression requires the regulated ectodomain cleavage of neuronal pentraxin NPR by TACE. Neuron 57, 858–871.

Csicsvari, J., Hirase, H., Czurkó, A., Mamiya, A., and Buzsáki, G. (1999a). Fast network oscillations in the hippocampal CA1 region of the behaving rat. J. Neurosci. 19, RC20.

Csicsvari, J., Hirase, H., Czurkó, A., Mamiya, A., and Buzsáki, G. (1999b). Oscillatory coupling of hippocampal pyramidal cells and interneurons in the behaving Rat. J. Neurosci. 19, 274–287.

Doischer, D., Hosp, J.A., Yanagawa, Y., Obata, K., Jonas, P., Vida, I., and Bartos, M. (2008). Postnatal differentiation of basket cells from slow to fast signaling devices. J. Neurosci. 28, 12956–12968.

Du, J., Zhang, L., Weiser, M., Rudy, B., and McBain, C.J. (1996). Developmental expression and functional characterization of the potassium-channel subunit Kv3.1b in parvalbumin-containing interneurons of the rat hippocampus. J. Neurosci. 16, 506–518.

Ellender, T.J., Nissen, W., Colgin, L.L., Mann, E.O., and Paulsen, O. (2010). Priming of hippocampal population bursts by individual perisomatic-targeting interneurons. J. Neurosci. 30, 5979–5991.

Fazzari, P., Paternain, A.V., Valiente, M., Pla, R., Luján, R., Lloyd, K., Lerma, J., Marín, O., and Rico, B. (2010). Control of cortical GABA circuitry development by Nrg1 and ErbB4 signalling. Nature 464, 1376–1380.

Foster, D.J., and Wilson, M.A. (2006). Reverse replay of behavioural sequences in hippocampal place cells during the awake state. Nature 440, 680–683.

Fuchs, E.C., Zivkovic, A.R., Cunningham, M.O., Middleton, S., Lebeau, F.E., Bannerman, D.M., Rozov, A., Whittington, M.A., Traub, R.D., Rawlins, J.N., and Monyer, H. (2007). Recruitment of parvalbumin-positive interneurons determines hippocampal function and associated behavior. Neuron 53, 591–604.

Gabernet, L., Jadhav, S.P., Feldman, D.E., Carandini, M., and Scanziani, M. (2005). Somatosensory integration controlled by dynamic thalamocortical feed-forward inhibition. Neuron 48, 315–327.

Geiger, J.R., Melcher, T., Koh, D.S., Sakmann, B., Seeburg, P.H., Jonas, P., and Monyer, H. (1995). Relative abundance of subunit mRNAs determines gating and Ca2+ permeability of AMPA receptors in principal neurons and interneurons in rat CNS. Neuron 15, 193–204.

Geiger, J.R., Lübke, J., Roth, A., Frotscher, M., and Jonas, P. (1997). Submillisecond AMPA receptor-mediated signaling at a principal neuron-interneuron synapse. Neuron 18, 1009–1023.

Gogolla, N., Caroni, P., Lüthi, A., and Herry, C. (2009). Perineuronal nets protect fear memories from erasure. Science 325, 1258–1261.

Goldberg, E.M., Jeong, H.Y., Kruglikov, I., Tremblay, R., Lazarenko, R.M., and Rudy, B. (2011). Rapid developmental maturation of neocortical FS cell intrinsic excitability. Cereb. Cortex 21, 666–682.

Gu, Y., Huang, S., Chang, M.C., Worley, P., Kirkwood, A., and Quinlan, E.M. (2013). Obligatory role for the immediate early gene NARP in critical period plasticity. Neuron 79, 335–346.

Hefft, S., and Jonas, P. (2005). Asynchronous GABA release generates long-lasting inhibition at a hippocampal interneuron-principal neuron synapse. Nat. Neurosci. 8, 1319–1328.

Klausberger, T., and Somogyi, P. (2008). Neuronal diversity and temporal dynamics: the unity of hippocampal circuit operations. Science 321, 53–57.

Klausberger, T., Roberts, J.D., and Somogyi, P. (2002). Cell type- and input-specific differences in the number and subtypes of synaptic GABA(A) receptors in the hippocampus. J. Neurosci. 22, 2513–2521.

Koch, S.M., and Ullian, E.M. (2010). Neuronal pentraxins mediate silent synapse conversion in the developing visual system. J. Neurosci. 30, 5404–5414.

Korotkova, T., Fuchs, E.C., Ponomarenko, A., von Engelhardt, J., and Monyer, H. (2010). NMDA receptor ablation on parvalbumin-positive interneurons impairs hippocampal synchrony, spatial representations, and working memory. Neuron 68, 557–569.

Krook-Magnuson, E., Armstrong, C., Oijala, M., and Soltesz, I. (2013). On-demand optogenetic control of spontaneous seizures in temporal lobe epilepsy. Nat. Commun. 4, 1376.

Lee, S.H., Földy, C., and Soltesz, I. (2010). Distinct endocannabinoid control of GABA release at perisomatic and dendritic synapses in the hippocampus. J. Neurosci. 30, 7993–8000.

Maheshwari, A., Nahm, W.K., and Noebels, J.L. (2013). Paradoxical proepileptic response to NMDA receptor blockade linked to cortical interneuron defect in stargazer mice. Front. Cell. Neurosci. 7, 156.

Mann, E.O., Suckling, J.M., Hajos, N., Greenfield, S.A., and Paulsen, O. (2005). Perisomatic feedback inhibition underlies cholinergically induced fast network oscillations in the rat hippocampus in vitro. Neuron 45, 105–117.

Mi, R., Tang, X., Sutter, R., Xu, D., Worley, P., and O'Brien, R.J. (2002). Differing mechanisms for glutamate receptor aggregation on dendritic spines and shafts in cultured hippocampal neurons. J. Neurosci. 22, 7606–7616.

Morozov, Y.M., and Freund, T.F. (2003). Postnatal development and migration of cholecystokinin-immunoreactive interneurons in rat hippocampus. Neuroscience 120, 923–939.

Murray, A.J., Sauer, J.F., Riedel, G., McClure, C., Ansel, L., Cheyne, L., Bartos, M., Wisden, W., and Wulff, P. (2011). Parvalbumin-positive CA1 interneurons are required for spatial working but not for reference memory. Nat. Neurosci. 14, 297–299.

O'Brien, R.J., Xu, D., Petralia, R.S., Steward, O., Huganir, R.L., and Worley, P. (1999). Synaptic clustering of AMPA receptors by the extracellular immediate-early gene product Narp. Neuron 23, 309–323.

O'Brien, R., Xu, D., Mi, R., Tang, X., Hopf, C., and Worley, P. (2002). Synaptically targeted narp plays an essential role in the aggregation of AMPA receptors at excitatory synapses in cultured spinal neurons. J. Neurosci. 22, 4487–4498.

Okaty, B.W., Miller, M.N., Sugino, K., Hempel, C.M., and Nelson, S.B. (2009). Transcriptional and electrophysiological maturation of neocortical fast-spiking GABAergic interneurons. J. Neurosci. 29, 7040–7052.

Owen, S.F., Tuncdemir, S.N., Bader, P.L., Tirko, N.N., Fishell, G., and Tsien, R.W. (2013). Oxytocin enhances hippocampal spike transmission by modulating fast-spiking interneurons. Nature 500, 458–462.

Paz, J.T., Bryant, A.S., Peng, K., Fenno, L., Yizhar, O., Frankel, W.N., Deisseroth, K., and Huguenard, J.R. (2011). A new mode of corticothalamic transmission revealed in the Gria4(-/-) model of absence epilepsy. Nat. Neurosci. 14, 1167–1173.

Petroski, R.E., Pomeroy, J.E., Das, R., Bowman, H., Yang, W., Chen, A.P., and Foster, A.C. (2006). Indiplon is a high-affinity positive allosteric modulator with selectivity for alpha1 subunit-containing GABAA receptors. J. Pharmacol. Exp. Ther. 317, 369–377.

Pizzorusso, T., Medini, P., Berardi, N., Chierzi, S., Fawcett, J.W., and Maffei, L. (2002). Reactivation of ocular dominance plasticity in the adult visual cortex. Science 298, 1248–1251.

Pouille, F., and Scanziani, M. (2001). Enforcement of temporal fidelity in pyramidal cells by somatic feed-forward inhibition. Science *293*, 1159–1163.

Rácz, A., Ponomarenko, A.A., Fuchs, E.C., and Monyer, H. (2009). Augmented hippocampal ripple oscillations in mice with reduced fast excitation onto parvalbumin-positive cells. J. Neurosci. *29*, 2563–2568.

Seto-Ohshima, A., Aoki, E., Semba, R., Emson, P.C., and Heizmann, C.W. (1990). Appearance of parvalbumin-specific immunoreactivity in the cerebral cortex and hippocampus of the developing rat and gerbil brain. Histochemistry *94*, 579–589.

Shevtsova, O., and Leitch, B. (2012). Selective loss of AMPA receptor subunits at inhibitory neuron synapses in the cerebellum of the ataxic stargazer mouse. Brain Res. *1427*, 54–64.

Sia, G.M., Béïque, J.C., Rumbaugh, G., Cho, R., Worley, P.F., and Huganir, R.L. (2007). Interaction of the N-terminal domain of the AMPA receptor GluR4 subunit with the neuronal pentraxin NP1 mediates GluR4 synaptic recruitment. Neuron *55*, 87–102.

Spiegel, I., Mardinly, A.R., Gabel, H.W., Bazinet, J.E., Couch, C.H., Tzeng, C.P., Harmin, D.A., and Greenberg, M.E. (2014). Npas4 regulates excitatory-inhibitory balance within neural circuits through cell-type-specific gene programs. Cell *157*, 1216–1229.

Tao, Y., Chen, Y.J., Shen, C., Luo, Z., Bates, C.R., Lee, D., Marchetto, S., Gao, T.M., Borg, J.P., Xiong, W.C., and Mei, L. (2013). Erbin interacts with TARP γ-2 for surface expression of AMPA receptors in cortical interneurons. Nat. Neurosci. *16*, 290–299.

Ting, A.K., Chen, Y.J., Wen, L., Yin, D.M., Shen, C.Y., Tao, Y.M., Liu, X.H., Xiong, W.C., and Mei, L. (2011). Neuregulin 1 promotes excitatory synapse development and function in GABAergic interneurons. J. Neurosci. *31*, 15–25.

Tomita, S., Chen, L., Kawasaki, Y., Petralia, R.S., Wenthold, R.J., Nicoll, R.A., and Bredt, D.S. (2003). Functional studies and distribution define a family of transmembrane AMPA receptor regulatory proteins. J. Cell Biol. *161*, 805–816.

Traynelis, S.F., and Dingledine, R. (1988). Potassium-induced spontaneous electrographic seizures in the rat hippocampal slice. J. Neurophysiol. *59*, 259–276.

Tricoire, L., Pelkey, K.A., Daw, M.I., Sousa, V.H., Miyoshi, G., Jeffries, B., Cauli, B., Fishell, G., and McBain, C.J. (2010). Common origins of hippocampal Ivy and nitric oxide synthase expressing neurogliaform cells. J. Neurosci. *30*, 2165–2176.

Tsui, C.C., Copeland, N.G., Gilbert, D.J., Jenkins, N.A., Barnes, C., and Worley, P.F. (1996). Narp, a novel member of the pentraxin family, promotes neurite outgrowth and is dynamically regulated by neuronal activity. J. Neurosci. *16*, 2463–2478.

Varga, C., Golshani, P., and Soltesz, I. (2012). Frequency-invariant temporal ordering of interneuronal discharges during hippocampal oscillations in awake mice. Proc. Natl. Acad. Sci. USA *109*, E2726–E2734.

Varga, C., Oijala, M., Lish, J., Szabo, G.G., Bezaire, M., Marchionni, I., Golshani, P., and Soltesz, I. (2014). Functional fission of parvalbumin interneuron classes during fast network events. Elife *3*, http://dx.doi.org/10.7554/eLife.04006.

Xu, D., Hopf, C., Reddy, R., Cho, R.W., Guo, L., Lanahan, A., Petralia, R.S., Wenthold, R.J., O'Brien, R.J., and Worley, P. (2003). Narp and NP1 form heterocomplexes that function in developmental and activity-dependent synaptic plasticity. Neuron *39*, 513–528.

Zhu, J.J., Esteban, J.A., Hayashi, Y., and Malinow, R. (2000). Postnatal synaptic potentiation: delivery of GluR4-containing AMPA receptors by spontaneous activity. Nat. Neurosci. *3*, 1098–1106.